AGU PUBLICATIONS

Global Biogeochemical Cycles

RESEARCH ARTICLE
10.1002/2017GB005759

Key Points:
- The Midwestern Corn/Soybean Belt is a hot spot for N_2O emissions and accounts for 30% of total emissions from North America
- Half of annual N_2O emissions from this belt occurs between April and July, corresponding to the time of spring N fertilizer application
- About 2.2-2.4% of N inputs to the corn/soybean belt, including soybean N_2 fixation and synthetic and organic N fertilizer, are emitted as N_2O

Supporting Information:
- Supporting Information S1

Correspondence to:
C. Nevison,
cynthia.nevison@colorado.edu

Citation:
Nevison, C., Andrews, A., Thoning, K., Dlugokencky, E., Sweeney, C., Miller, S., et al. (2018). Nitrous oxide emissions estimated with the CarbonTracker-Lagrange North American regional inversion framework. *Global Biogeochemical Cycles*, *32*, 463–485. https://doi.org/10.1002/2017GB005759

Received 7 JUL 2017
Accepted 23 FEB 2018
Accepted article online 1 MAR 2018
Published online 23 MAR 2018

Nitrous Oxide Emissions Estimated With the CarbonTracker-Lagrange North American Regional Inversion Framework

Cynthia Nevison[1], Arlyn Andrews[2], Kirk Thoning[2], Ed Dlugokencky[2], Colm Sweeney[2], Scot Miller[3], Eri Saikawa[4], Joshua Benmergui[5], Marc Fischer[6], Marikate Mountain[7], and Thomas Nehrkorn[7]

[1]University of Colorado Boulder/INSTAAR, Boulder, CO, USA, [2]NOAA ESRL Global Monitoring Division, Boulder, CO, USA, [3]Department of Global Ecology, Carnegie Institution for Science, Stanford, CA, USA, [4]Department of Environmental Sciences, Emory University, Atlanta, GA, USA, [5]Harvard John A. Paulson School of Engineering and Applied Sciences, Cambridge, MA, USA, [6]Lawrence Berkeley National Laboratory, Berkeley, CA, USA, [7]Atmospheric and Environmental Research, Lexington, MA, USA

Abstract North American nitrous oxide (N_2O) emissions of 1.6 ± 0.3 Tg N/yr over 2008–2014 are estimated using the CarbonTracker-Lagrange regional inversion framework. The estimated N_2O emissions are largely consistent with the EDGAR (Emission Database for Global Atmospheric Research) global inventory and with the results of global atmospheric inversions but offer more spatial and temporal detail over North America. Emissions are strongest from the Midwestern Corn/Soybean Belt, which accounts for nearly one third of the total North American N_2O source. The emissions are maximum in spring/early summer, consistent with a nitrogen fertilizer-driven source, and also show a late winter spike suggestive of freeze-thaw effects. Interannual variability in emissions across the primary months of fertilizer application is positively correlated to mean precipitation. The estimated N_2O flux from the Midwestern Corn/Soybean Belt and the more northerly United States/Canadian wheat belt corresponds to 4.2–4.6% and 2.2–3.0%, respectively, of total synthetic + organic N fertilizer applied to those regions. Consideration of nonagricultural sources and additional N inputs from soybean N_2 fixation could reduce the N_2O yield from the Midwestern Corn/Soybean Belt to ~2.2–2.4% of total N inputs.

Plain Language Summary Emissions of nitrous oxide (N_2O) emissions over North America were estimated based on an inverse model, in which atmospheric concentrations of N_2O measured at 40 different National Oceanographic Atmospheric Administration (NOAA) sites were "inverted" to estimate surface sources. The estimated N_2O emissions showed a clear hot spot in the Midwestern corn/soybean belt, which accounted for nearly one third ($0.48 \pm 0.02 \times 10^{12}$ g N/yr) of the total North American N_2O source ($1.6 \pm 0.3 \times 10^{12}$ g N/yr). The emissions were maximum in spring and early summer, consistent with the timing of nitrogen fertilizer application to the corn/soybean belt. Interannual variability across 2007–2015 in the inferred emissions suggested that climate may interact with fertilizer to influence N_2O source strength, with the warm drought year 2012 showing substantially lower emissions than other years.

1. Introduction

Nitrous oxide (N_2O) is a long-lived greenhouse gas that is produced in soils, freshwater, and oceans by microbes that rely on nitrogen (N) substrates for their energetic metabolism. N_2O subsequently is destroyed in the stratosphere, mainly by photolysis to N_2, but a fraction is oxidized to NO_x, which is a catalyst of stratospheric ozone depletion (Ravishankara et al., 2009). The abundance of N_2O in the atmosphere has increased by about 20% over preindustrial levels, from 275 ppb to a mean of 329 ppb in 2016 (MacFarling-Meure et al., 2006; NOAA GMD, 2017). This increase is estimated to have caused about 6% of the total enhanced anthropogenic greenhouse gas radiative forcing in 2015 (update of Hofmann et al., 2006). The increase in N_2O has been driven largely by industrial synthetic N fertilizer production, which, together with the combustion of fossil fuels and cultivation of N_2 fixing crops, has more than doubled reactive N inputs to terrestrial ecosystems since preindustrial times (Crutzen et al., 2008; Galloway et al., 2004; Vitousek et al., 1997). The role of synthetic N fertilizer as the main overall driver of the N_2O increase is supported by the observed isotopic lightening in the $\delta^{15}N$ signature of tropospheric N_2O over the past century (Park et al., 2012). However, other disturbances, including tilling, livestock grazing, deforestation, and climate change, have accelerated natural N cycling and likely are also contributing to enhanced N_2O emissions (Davidson, 2009; Saikawa et al., 2013).

The question of what fraction of synthetic N fertilizer is ultimately released as N_2O is one of long-standing interest in the atmospheric sciences (Crutzen, 1974, 1976, 2008; Nevison & Holland, 1997). This question was originally addressed with a global-scale mass balance approach based on the assumption that anthropogenically fixed N eventually must be returned to the atmosphere by denitrifying microbes. The reasoning was that some fraction of that denitrified N inevitably leaks off as N_2O rather than being reduced all the way to N_2 (Crutzen, 1976; McElroy & Wofsy, 1976). This big picture approach gave way to bottom-up calculations, based on extrapolation of chamber measurements of N_2O emissions, which concluded that only about 1% of fertilizer was lost as N_2O directly from fertilized fields (Bouwman et al., 1995; Eichner, 1990). More recently, a renewed application of the top-down approach, based on comparing the increase in atmospheric N_2O since the preindustrial era to the increased reactive N input from anthropogenic N_2 fixation, suggested that 3–5% of synthetic fertilizer ultimately is emitted as N_2O (Crutzen et al., 2008). Another study, using a similar global box model approach but distinguishing newly fixed synthetic versus recycled organic (i.e., manure-based) N fertilizers, derived N_2O emission coefficients of 2.5% and 2%, respectively, for synthetic and organic fertilizers (Davidson, 2009).

The top-down box model approaches have been largely reconciled with more recent bottom-up calculations with the recognition that the ultimate N_2O emission associated with fertilizer is greater than that observed directly from the field. Rather, additional microbial N_2O production can occur due to downstream or cascading effects as N is leached, volatilized and redeposited, and consumed by livestock and humans (Mosier et al., 1998). The concept of the N cascade is captured in the current Intergovernmental Panel on Climate Change (IPCC) methodology for quantifying national greenhouse gas emissions. While the IPCC methodology still assumes only a 1% direct emission coefficient for fertilizer applied to agricultural land, it also defines a further set of N_2O emission factors applied to a suite of other agricultural N fluxes, including manure production and management, crop N_2 fixation, and leaching and subsequent runoff in rivers to coastal zones. This cradle-to-grave (i.e., N_2 fixation to denitrification) approach to N accounting has brought global-scale bottom-up N_2O budgets into approximate balance with the observed increase in atmospheric N_2O (Ciais et al., 2013; Mosier et al., 1998).

Meanwhile, atmospheric N_2O data at high spatial and temporal resolution have become increasingly available in recent years from aircraft campaigns and global and regional monitoring networks (Francey et al., 2003; Hirsch et al., 2006; Prinn et al., 2000; Sweeney et al., 2015; Thompson et al., 2004). These data have been used in several recent global atmospheric inversions, which have emphasized the importance of the tropics as the primary source of N_2O and identified Asia as a region of rapidly growing N_2O emissions (Hirsch et al., 2006; Huang et al., 2008; Saikawa et al., 2014; Thompson et al., 2014).

In addition to the global studies, a number of regional atmospheric inversions have sought to quantify N_2O emissions from North America (Chen et al., 2016; Fu et al., 2017; Kort et al., 2008, 2010; Miller et al., 2012; Xiang et al., 2013) and Europe (Corazza et al., 2011; Ganesan et al., 2015; Manning et al., 2011). The North American studies have evaluated global inventories such as (Emission Database for Global Atmospheric Research) EDGAR, which use an emission factor approach similar to that of the IPCC national greenhouse gas emissions methodology, and have concluded that these inventories underestimate the true U.S. anthropogenic N_2O source by a factor of 3 or more. However, this result has been based on a limited number of atmospheric observations, restricted in some cases to May–June of a single year, and the studies have noted that more information about the seasonality in emissions would be valuable for constraining the annual mean N_2O source. To date, the most comprehensive regional N_2O inversion over North America was based on data collected in 2008 from four tower sites in Wisconsin, Iowa, Colorado, and Texas. That study found strong seasonality in the N_2O emissions, peaking in May/June, with an estimated total annual source from North America of 2.1–2.6 Tg N/yr (Miller et al., 2012).

Here we present results of a recently developed regional inversion methodology for North America (Hu et al., 2015). Compared to previous regional N_2O inversions, the new study uses a substantially larger set of measurement sites, encompassing 25 surface-based and 15 aircraft-based sites from the National Oceanic and Atmospheric Administration (NOAA) and partners. The time period of the inversion is longer and more seasonally comprehensive than in past regional studies. It extends from 1 January 2007 to 31 December 2015, with a focus on the central years 2008–2014. We apply the inversion to quantify and characterize the spatial distribution, overall magnitude, seasonality, and interannual variability in North American N_2O emissions. In addition, we focus on specific regions, particularly the Midwestern Corn/Soybean Belt, to address the fraction of fertilizer emitted as N_2O and the plausibility that the EDGAR inventory could be underestimating U.S. N_2O emissions by a factor of 3.

Table 1
Information on N_2O Measurement Sites Used in the Inversion

Site	Latitude (°N)	Longitude (°W)	Altitude meters above ground level	Number of measurements	Data period
			Surface sites		
AMT	45.0	68.7	107	1,460	1/7–12/15
BAO	40.1	105.0	300	2,880	8/7–12/15
BMW	32.3	64.9	30	341	1/7–12/15
BRW	71.3	156.6	17	933	1/7–12/15
CBA	55.2	162.7	36	656	1/7–12/15
CRV	65.0	147.6	32	824	10/11–12/15
HSU	41.0	124.3	8	72	5/8–12/15
INX	39.6 to 39.9	86.4 to 85.7	156 to 225	1,168	10/10–12/15
KEY	25.7	80.2	5	394	1/7–12/15
LEF	45.9	90.3	244 or 396	3,138	1/7–12/15
LLB	55.0	112.5	48	193	1/8–2/13
MBO	44.0	121.7	11	629	10/11–5/14
MEX	19.0	97.3	4,469[a]	282	1/9–12/15
MLS	39.5 to 40.6	110.2 to 104.5	0 to 13	289	6/8–7/8 and 6/11–6/12
MWO	34.2	118.1	1,774[a]	2,040	4/10–12/15
NWR	40.0	105.6	3,526[a]	730	1/7–12/15
POC	10 to 35	145 to 118	20	258	1/7–1/12
SCT	33.4	81.8	305	1,867	8/8–12/15
SGP	36.6	97.5	60	452	1/7–12/15
STR	37.8	122.5	486[a]	4,036	10/7–12/15
THD	41.0	124.2	5	453	1/7–12/15
UTA	39.9	113.7	5	333	1/7–12/15
WBI	41.7	91.4	379	2,876	6/7–12/15
WGC	38.3 to 39.3	121.5	91	2,037	9/7–12/15
WKT	31.3	97.3	5, 122 or 457	2,427	1/7–12/15
			Aircraft sites		
ACG	57.0 to 76.6	169.7 to 131.8	883 to 7,969	1,382	6/9–9/15
CAR	40.1 to 40.9	105.2 to 104.1	665 to 6,658	2,246	1/7–12/15
CMA	38.4 to 39.0	76.5 to 74.1	284 to 7,422	1,858	1/7–12/15
DND	47.2 to 48.5	99.5 to 96.2	138 to 7,002	1,202	1/7–12/15
ESP	49.3 to 49.6	126.6 to 125.7	314 to 5,149	2,432	1/7–12/15
ETL	53.9 to 54.6	105.3 to 104.4	463 to 6,165	2,180	1/7–12/15
HIL	39.9 to 40.2	88.1 to 87.7	727 to 7,549	1,642	1/7–12/15
LEF	45.7 to 46.1	90.4 to 89.9	160 to 3,250	2,133	1/7–12/15
MLS	32.1 to 48.8	112.2 to 96.1	2 to 3,390	760	2/12–10/15
NHA	42.8 to 43.1	70.7 to 70.3	321 to 7,300	2,241	1/7–12/15
PFA	64.1 to 65.9	151.1 to 146.0	2,343 to 6,467	2,342	1/7–12/15
SCA	32.5 to 33/9	79.8 to 79.3	332 to 7,861	1,888	1/7–12/15
THD	40.9 to 41.6	124.4 to 123.9	311 to 7,901	1,236	1/7–12/15
TGC	27.4 to 27.9	97.0 to 96.5	317 to 7,893	1,434	1/7–12/15
WBI	41.6 to 42.5	91.9 to 91.1	372 to 6,372	1,376	1/7–12/15

[a]Above sea level.

2. Methods

2.1. Atmospheric N_2O Data

The regional inversion was based on atmospheric N_2O data from the NOAA Global Greenhouse Gas Reference Network (https://www.esrl.noaa.gov/gmd/ccgg/). NOAA's Carbon Cycle Greenhouse Gas group maintains a discrete air sampling network in which duplicate samples are collected in Teflon O-ring sealed glass flasks about weekly and shipped to the NOAA Earth System Research Laboratory in Boulder, Colorado, USA, for analysis of N_2O on a gas chromatograph with electron capture detection. Response of the electron capture detection to N_2O is calibrated with a suite of standards on the World Meteorological Organization X2006A scale maintained by NOAA (Hall et al., 2007). Tall towers (Andrews et al., 2014) and aircraft (Sweeney et al., 2015) in the Global Greenhouse Gas Reference Network use programmable 12-flask sampling systems. Air samples at tower sites are collected in midafternoon, with a typical

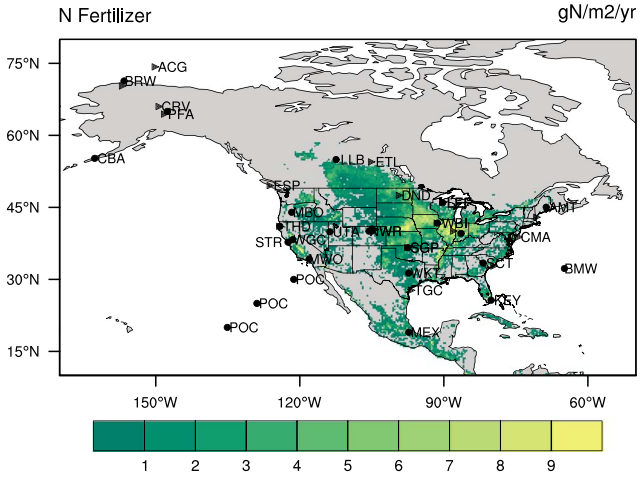

Figure 1. N_2O observation sites from National Oceanic and Atmospheric Administration Global Greenhouse Gas Reference Network (circles = surface-based and triangles = aircraft), superimposed on map of annual synthetic N fertilizer use from www.sage.wisc.edu. Where permitted by legibility, selected stations are labeled.

sampling frequency between 1 and 3 days. Several sites important for this study came online during summer/fall 2007 (WBI and WGC) and late summer 2008 (SCT). At aircraft profiling sites the units are deployed on small aircraft and samples are collected at different altitudes from ~500 m above ground level up to ~8,000 m above sea level. Sample collection takes less than a minute, so each measurement represents a nearly instantaneous sample. The reproducibility of the measurements, based on the mean of absolute values of differences from flask pairs for the inversion period (2007–2015, is 0.24 ppb. Table 1 and Figure 1 provide more details about the location of each site and the available time span of data within the inversion period.

2.2. Inversion Framework

The CarbonTracker-Lagrange (CT-L) regional inversion framework uses the Bayesian methodology and algorithms described by Yadav and Michalak (2013) to optimize fluxes by solving equation (1):

$$\hat{\mathbf{s}} = \mathbf{s_p} + (\mathbf{HQ})^{\mathsf{T}}\left(\mathbf{HQH^T} + \mathbf{R}\right)^{-1}\left(\mathbf{z} - \mathbf{Hs_p}\right) \quad (1)$$

where

$\hat{\mathbf{s}}_{(m\ x\ 1)}$ is the optimized surface flux in nmol m^{-2} s^{-1}.

$\mathbf{s_p}_{\ (m\ x\ 1)}$ is the prior estimate of **s**.

$\mathbf{z}_{(n\ x\ 1)}$ is a vector of N_2O observations, corrected by subtracting an empirical background value, in ppb.

$\mathbf{H}_{(n\ x\ m)}$ is a transport matrix, in ppb/(nmol m^{-2} s^{-1}) that describes the relationship between the surface fluxes **s** and the observations **z**.

$\mathbf{R}_{(n\ x\ n)}$ is the model-data mismatch error covariance matrix, in ppb^2.

$\mathbf{Q}_{(m\ x\ m)}$ is the prior flux covariance error matrix, in (nmol m^{-2} s^{-1})^2.

The dimensions of the equation are defined as follows:

$m =$ pr is the number of surface fluxes solved for, where p is the number of time steps and r is the number of spatial grid cells.

n is the number of atmospheric observations.

The flux vector **s** was defined at 1° × 1° resolution over North America. The original vector was an 80 × 120 matrix extending from 10° to 80°N and 170° to 50°W. This was subsequently reduced using a land mask to r = 3470 land grid cells, since the inversion only solves for terrestrial fluxes from within the CT-L domain. The inversion was run with a daily time step for each year from 1 January 2007 to 31 December 2015. For computational reasons, this 9 year time span was divided into nine separate, partly overlapping inversions centered around each calendar year. To avoid end effects, each calendar year was padded by one month by including the previous December (except in 2007) and the following January (except in 2015), such that the total number of time steps p was 427 or 428 for 2008–2014 (accounting for leap years in 2008 and 2012) and 396 in 2007 and 2015. The full dimension of $m = pr$ was thus ~1.48×10^6 for each of the seven fully padded 14 month inversions from 2008 to 2014 and 1.37×10^6 for the partly padded 13 month inversions in 2007 and 2015.

The technique of Yadav and Michalak (2013) avoids directly creating **Q** as a full m x m matrix. In this method, **Q** is computed as a function of the prior flux error vector $\boldsymbol{\sigma}_\mathbf{s}$ and the temporal covariance, $\mathbf{D}_{(p\ x\ p)} = \exp\left(-\frac{\mathbf{X}_\tau}{l_\tau}\right)$, and the spatial covariance, $\mathbf{E}_{(r\ x\ r)} = \exp\left(-\frac{\mathbf{X}_s}{l_s}\right)$, matrices.

$$\mathrm{Q} = \boldsymbol{\sigma}_\mathbf{s}\boldsymbol{\sigma}_\mathbf{s}^{\mathbf{T}} \circ \left[\exp\left(-\frac{\mathbf{X}_\tau}{l_\tau}\right)\right] \otimes \left[\exp\left(-\frac{\mathbf{X}_s}{l_s}\right)\right], \quad (2)$$

where ∘ denotes element by element multiplication (the Hadamard product) and ⊗ denotes the Kronecker product. Note that we do not compute $\boldsymbol{\sigma}_\mathbf{s}\boldsymbol{\sigma}_\mathbf{s}^{\boldsymbol{T}}$explicitly; instead, we modified the Yadav and Michalak (2013) algorithms such that $\boldsymbol{\sigma}_\mathbf{s}$ is allowed to vary in space and time and has the same m x 1 dimensions as the prior (details are available here: https://www.esrl.noaa.gov/gmd/ccgg/carbontracker-lagrange/doc/hsigma.

html#hsigma). $\mathbf{X_\tau}$ and $\mathbf{X_s}$ represent matrices of the separation lags/distances between estimation locations in time and space, respectively, and l_τ and l_s are the temporal and spatial correlation length parameters, in units of days and kilometers, respectively. The selection of values for $\boldsymbol{\sigma_s^2}$, l_τ, and l_s is discussed in section 2.4.

The construction of the transport matrix **H** began with the computation of footprints (*f*) for each of the *n* sampling events or "receptors" at all sites during 2007–2015. The footprints were computed with the Stochastic Time-Inverted Lagrangian Transport (STILT) model (Lin et al., 2003), which was driven by a Weather Research and Forecasting (WRF) model simulation customized for Lagrangian modeling (Nehrkorn et al., 2010). The WRF meteorology has nested domains with resolution of 10 km over the contiguous United States and much of Canada and 30–40 km over the rest of the North America and its surrounding oceans (Hegarty et al., 2013). While some previous inversions of N_2O and other trace gases have examined transport uncertainty by using two or more transport models to compute **H** (Hu et al., 2015; Miller et al., 2012), we focus here on STILT-WRF. Simulations were run for each receptor with an ensemble of 500 particles, which were transported backward in time for 10 days with hourly output. At any grid cell where one or more particles reached the lower half of the boundary layer, the influence footprint was calculated based on the number and duration of particles in the layer (Lin et al., 2003). The parameterizations in STILT are computationally expensive compared to other particle dispersion models such as Hybrid Single-Particle Lagrangian Integrated Trajectory (HYSPLIT) (Draxler & Hess, 1998; Stein et al., 2015) and the FLEXible PARTicle dispersion model (FLEXPART) (Stohl et al., 1998). Hegarty et al. (2013) compared STILT, HYSPLIT, and FLEXPART and showed that STILT performance was similar to the other models despite running with many fewer particles. With 500 particles, the footprint adequately resolves the near field (i.e., the first few days of backward transport) but becomes patchy as particles disperse widely after several days of transport. The limited number of particles likely causes some noise when footprints are convolved with gridded fluxes, but it should not introduce any systematic errors.

For use in the inversion, the data described in section 2.1 were filtered to remove all flasks collected 4,000 m or more above the local surface. These data generally had small surface influence footprints but were influenced occasionally by episodic stratospheric intrusions of highly N_2O-depleted air, which the inversion framework is not well equipped to handle. An additional filter was applied to flasks collected during the nighttime or early morning, due to the difficulty of modeling the height of the nighttime planetary boundary layer. In an effort to retain as many data as possible, this filter was only applied in the warm season, which was defined as a function of latitude. Sites north of 60°, which are always cold, were excluded from the filter, as were high altitude and other sites where the sampling protocol routinely involves nighttime collection.

2.3. Prior Fluxes

Our standard prior was adapted from the posterior flux of the global atmospheric N_2O inversion of Saikawa et al. (2014). The latter was an independent Bayesian inversion spanning 1995–2008, which used the Model of OZone and Related Tracers (MOZART) v4 atmospheric transport model at 1.9° latitude × 2.5° longitude and all available observations from several different global monitoring networks, including 18 of the surface sites used in the current study. To ensure that the data used here are independent, we used the Saikawa et al. (2014) result for 2000 as the prior flux for all years of our 2007–2015 regional inversion.

The Saikawa et al. prior fluxes included a combination of inventory-based industrial and agricultural soil emissions from EDGAR v4.1, biomass burning emissions from Global Fire Emissions Database v3, model-based natural soil emissions (Saikawa et al., 2013), and model-based oceanic emissions Manizzap et al. (2012). All of the input fluxes had monthly resolution, except for the EDGAR emissions, which had annual resolution (EDGAR, 2009). The global posterior fluxes were resolved annually by source type in that study, but the monthly seasonality of the Saikawa et al. (2014) prior fluxes was reimposed on the global posterior fluxes for use as our input prior to the regional inversion.

In addition to the standard prior described above, we repeated all simulations with a flat (i.e., noninformative) prior, uniform in time and space. The flat prior was designed such that its annual integrated total over the land-masked area of the CT-L domain was equal to that of the standard prior.

2.4. Model-Data Mismatch and Prior Flux Covariance Errors

Measurements of N_2O are very precise, with average agreement among paired flask-air samples during 2008 to 2014 of 0.24 ppb (0.1%). The model-data mismatch error **R** is therefore likely dominated by model errors

Table 2
Covariance Parameters Optimized Using Maximum Likelihood Estimation

Case	Spatial correlation length l_s (km)	Temporal correlation length l_τ (days)	Model-data mismatch σ_r (ppb)	Prior uncertainty $\sigma_s = b^*s_p + c$ (nmol/m^2/s)
1	300	35	0.84	$b = 1.5$, $c = 0.1$
2	300	35	0.75	$b = 4$, $c = 0.2$

associated with planetary boundary layer height, transport of trace species, background concentration, aggregation (i.e., solving fluxes on a finite grid), and representation (i.e., the effect of the finite emissions and meteorological grids on the modeled concentration). Uncertainties in the background values, which are presubtracted from the N_2O observations, as discussed below in section 2.5, also contribute substantially to **R**. We assumed that model-data mismatch errors were uncorrelated and that all observations used in the analysis provided independent information about fluxes. The flask observations are sufficiently separated in time and space as to make this uncorrelated approximation reasonable. The surface sites are generally several hundred kilometers apart, such that errors in atmospheric transport that covary at smaller scales will not affect the inversion. Hence, a diagonal matrix **R** is a reasonable approximation of the model-data mismatch errors.

The main diagonal components σ_r^2 of **R**, as well as the parameters l_τ and l_s and the vector $\boldsymbol{\sigma_s}$ used in the prior flux error matrix **Q**, were chosen with guidance from the maximum likelihood estimation (MLE) method (Michalak et al., 2005). Focusing first on the parameters l_s and l_τ, MLE suggested optimal values of 300 km and 35 days, respectively. With l_s and l_τ fixed at those values, we used the MLE method to explore a range of combinations of $\boldsymbol{\sigma_s}$ and σ_r, with the goal of finding an optimal balance between the $\mathbf{HQH^T}$ and **R** terms in equation (1). Here the range considered for σ_r was 0.6 to 1.2 ppb and the square root of the prior variance matrix $\boldsymbol{\sigma_s}$ was estimated as a scalar multiple b of the standard prior $\mathbf{s_p}$, plus an added constant c. While the MLE method did not give a definitive answer for all subsets of the N_2O observations considered (see section 4.5.4 for more details), it suggested two alternative sets of parameters, which we list in Table 2 as Cases 1 and 2. These cases span a reasonable range of parameter choices representing alternative scenarios of tighter prior/looser model-data mismatch and looser prior/tighter model-data mismatch. We performed repeat simulations with each set of parameters, with both the standard and flat (i.e., noninformative) priors, for a total of four permutations per year over the 9 years of the inversion. These are referred to hereafter as Case 1, Case 2, Case 1f, and Case 2f, where the latter two cases use the flat prior. Other inversions with smaller, coarser domains have rerun their model a large number of times (e.g., 50,000), sampling different covariance matrix parameters each time (Ganesan et al., 2014). However, a large number of simulations would be computationally unfeasible for the setup here; one padded yearly run of the inverse model requires 3–4 h. Instead, we use the spread in the results among the four simulations to approximate a range of uncertainties in the posterior fluxes due to the choice of prior and covariance matrix parameters. We also conducted sensitivity tests for the central years (2008–2014) of the inversion using the Case 1 parameters and standard priors but selectively removing station WBI in Iowa. These simulations are referred to as Case 1xwbi and were performed to examine the influence of WBI, where large seasonal enhancements in atmospheric N_2O are routinely detected, on the inversion results in the Midwest.

Finally, for each simulation we computed a regionally aggregated posterior flux covariance matrix to estimate the uncertainty in the aggregated fluxes from five regions of interest, defined below, which we report separately from the uncertainty described above associated with varying the prior and input parameters. The posterior flux covariance matrix is computed as a function of **Q**, **H**, and **R** (e.g., Yadav & Michalak, 2013) and is often considered a measure of random uncertainty. In practice, it includes a combination of random uncertainties, such as random measurement error, random transport error, and the sparsity of the observation network, and may also include some systematic errors (e.g., in the meteorology or the boundary condition) that may not be fully accounted for (e.g., Gourdji et al., 2012; Stephens et al., 2007).

2.5. Background Values

The atmospheric N_2O observations were adjusted by subtracting an empirically determined background value to compute the vector **z**. The background value was estimated based on the intersection of the STILT-WRF back trajectories used to compute the footprint with a four-dimensional time-varying field (with

5° × 5° × 1 km × 1 day resolution) covering North America and its surrounding oceans. The method for constructing the 4-D field, which is based on NOAA surface and aircraft N_2O data, is described in more detail in the supporting information. Briefly, data were categorized as marine boundary layer, free tropospheric, or continental boundary layer, depending on the location of each sample. These three categories were treated individually as follows. For the marine boundary layer, time- and latitude-dependent reference surfaces were computed separately for the Pacific and Atlantic (Masarie & Tans, 1995, updated as described https://www.esrl.noaa.gov/gmd/ccgg/mbl/). For the free-troposphere, reference surfaces were created using a similar approach, with an additional "domain-filling" step informed by backward and forward trajectories for each aircraft sample collected above 3,000 m above ground level. For the continental boundary layer, N_2O data were de-trended by subtracting the latitude- and time-dependent marine boundary layer reference values, where the transition from Pacific to Atlantic was represented by linear interpolation as a function of longitude across the continent. A multiyear mean seasonal cycle then was computed as a function of latitude, longitude, and day of year using local Kriging following Hammerling et al. (2012).

Background values for each individual N_2O measurement (i.e., receptor) were obtained by first determining endpoints for each of the 500 STILT-WRF particle back trajectories for that receptor. The 4-D North American N_2O field was sampled at these trajectory endpoints and a mean value and mean uncertainty (reflecting the uncertainty of the field at each endpoint location) were computed along with a standard error over the 500 trajectory endpoints (reflecting the spread of the N_2O values assigned to each endpoint) for each footprint. The mean uncertainty and the standard error were added in quadrature to produce an overall uncertainty estimate for each background value, which was typically around ±0.2 ppb.

According to the trajectory model, the air mass concentration is unchanged once a particle stops interacting with the surface fluxes. We therefore identified all the back trajectory waypoints after an individual particle exited the flux estimation domain (i.e., the North American continental boundary layer). The last waypoint (typically the most distant), restricted by a continental super land mask that limited the endpoint selection to grid cells within 4° of the North American continent, was selected as the point of intersection with the 4-D background field. Typically, about 80% ± 10% of particles exited over the ocean within 10 days, 10% ± 5% exited into the continental free troposphere, and 10% ± 6% remained within the continental boundary layer at the end of the 10 day back trajectory run.

2.6. Agricultural Data Sets

2.6.1. Crop Area Coverage

In our analysis of the posterior inversion fluxes, we used the agricultural data set described in Levis et al. (2012) to identify regions of particular interest with respect to N_2O emissions. The Levis et al. data set was adapted from earlier work by Ramankutty and Foley (1998) and is in units of percentage of total grid area planted in major crop types on a 0.5° × 0.5° global grid, which we interpolated to the CT-L domain. We focused on three main crop types: corn, soybean, and wheat, which together account for approximately 80% of agricultural land coverage in North America (Food and Agriculture Organization of the United Nations (FAO), 2016). Since the land area used for corn and soybean overlaps substantially, we consolidated these crops into a single category designated as corn/soybean (Figure 2). The crop area data set was used to define two North American regions of special interest, which we called the Midwestern Corn/Soybean Belt and the Northern Wheat Belt. These were delineated based on mutually exclusive latitude/longitude bounds, with the caveat that some wheat is grown in the corn/soybean belt and vice versa:

Midwestern Corn/Soybean: 36°N to 47°N, −102° to −80°W.
Northern Wheat: 47° to 54°N, −115° to −95°W.

Because wheat and corn/soybean crops also are grown outside of these latitude/longitude bounds, we defined two additional regions, All Corn/Soybean and All Wheat, which were delineated by a crop mask requiring that at least 5% of the area be covered in the respective crop. These latter regions were made mutually exclusive by requiring that the percentage of land in corn/soybean be greater than the percentage of land in wheat in the All Corn/Soybean region, and vice versa for the All Wheat region. Finally, we defined a region for California, which produces much of the nation's fruit and vegetables. This region was delineated by geographical state boundaries, since our inversion currently is not able to isolate agricultural emissions from other N_2O source types in California.

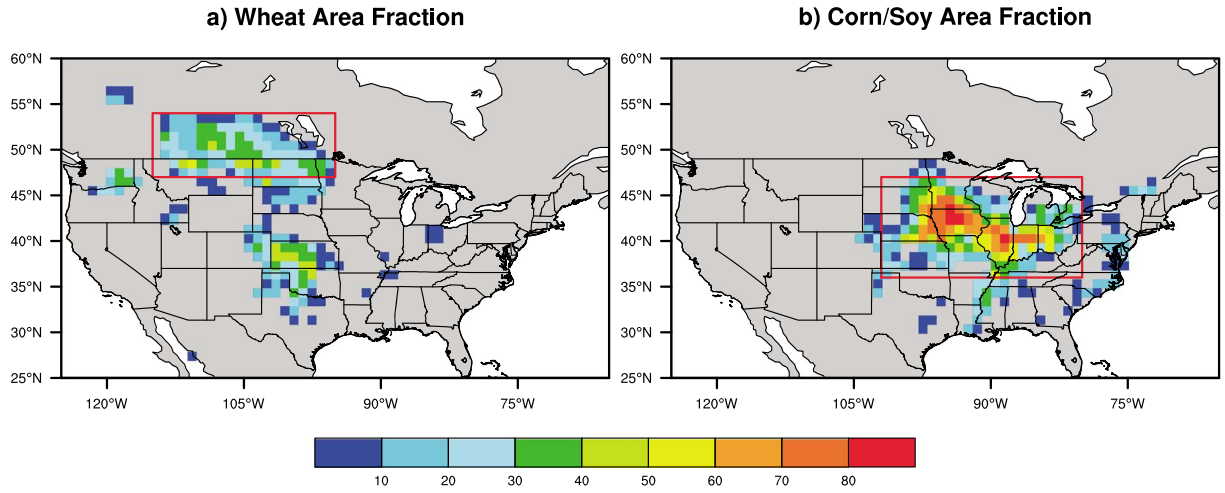

Figure 2. Percentage of total land area on the 1° × 1° CarbonTracker-Lagrange grid planted in (a) wheat, (b) corn, and/or soybean, limited to grid cells with a minimum of 5% coverage of each respective crop. Red boxes in Figures 2a and 2b delineate the Northern Wheat and Midwestern Corn/Soybean regions, respectively.

2.6.2. N Inputs

Synthetic and organic (i.e., manure) N fertilizer application, representing conditions circa year 2000, were obtained as separate global 0.5° × 0.5° maps from Potter et al. (2010). An alternative map of synthetic N fertilizer at 5 min resolution was obtained from the center for Sustainability and the Global Environment (SAGE) at the University of Wisconsin (www.sage.uwisc.edu). The Potter et al. and SAGE synthetic N data sets differ substantially in their North American totals of 12.9 and 14.8 Tg N/yr, respectively. The North American total organic fertilizer input from Potter et al. is 16.9 Tg N/yr. The agricultural N inputs to the corn/soybean and wheat regions were calculated for each of these three N fertilizer data sets using the crop area masks described in section 2.6.1 (Table 3). (Note that SAGE does not provide an organic fertilizer data set.)

Information on the seasonal timing of N fertilizer application in North America is not as readily available as the information on its spatial distribution, but personal communications from two agricultural university extension offices provide some rough guidelines. In the Midwestern Corn/Soybean Belt, the major N fertilizer applications typically occur twice in spring and once in fall. The spring applications include a preplant application around early April, when soils become fit for field work, and a late May/early June "sidedress" application, when the crop is growing but still small enough for farm machinery to get through (J. E. Sawyer, Iowa State University Extension, personal communication, 2016). Manure and anhydrous ammonia are applied in late fall prior to freezing but after temperatures have dropped below 10°C (50°F), with the goal of minimizing NH_3 volatilization losses. Major fertilizer applications to northern wheat crops include spring preplant and late fall manure/anhydrous ammonia. Here the timing of the preplant may vary widely from year to year, as the planting season can swing from early April to mid-June depending on the spring. The May/June sidedress application described for corn/soybean is much less common for wheat, although some growers apply N fertilizer at postflowering (late June/early July) to boost wheat protein (L. Lubenow, North Dakota State University Extension, personal communication, 2016).

2.7. North American Regional Reanalysis Data Sets

To investigate possible climate-related drivers of interannual variability in the posterior N_2O flux, focusing on the Midwestern Corn/Soybean Belt, we examined selected meteorological variables from the North American Regional Reanalysis (NARR) (Mesinger et al., 2006; National Centers for Environmental Prediction, 2016). These variables included precipitation, soil temperature (which differed little from air temperature), and soil moisture. Monthly mean values were downloaded on the NARR 32 km Lambert grid and were integrated over the Midwestern Corn/Soybean Belt. We computed regional monthly mean NARR integrals using the prescribed latitude/longitude bounds defined above for this belt.

To examine interannual variability over as many years as possible, we used N_2O inversion results spanning 2007–2015, keeping in mind that the January 2007 and December 2015 results likely included end effects, since they were not padded by 1 month on either end as were the 2008–2014 inversions. Furthermore,

Table 3
Mean Annual N_2O Fluxes and Applied N Fertilizers by Region (Tg N/yr)

Case	Description	Whole CT-L domain	Midwest Corn/Soybean 102°–80°W, 36°–47°N	All Corn/Soybean crop area filter	Northern Wheat 115°–95°W, 47°–54°N	All Wheat crop area filter
1	Standard prior	1.53 ± 0.09 (±0.004) ±0.3[a]	0.489 ± 0.040 (±0.015) ±0.02[a]	0.461 ± 0.038 (±0.016)	0.097 ± 0.022 (±0.025) ±0.03[a]	0.181 ± 0.029 (±0.016)
2	Standard prior	1.46 ± 0.08 (±0.007)	0.470 ± 0.039 (±0.024)	0.451 ± 0.029 (±0.026)	0.088 ± 0.029 (±0.039)	0.156 ± 0.039 (±0.027)
1f	Flat prior	1.70 ± 0.09 (±0.004)	0.474 ± 0.040 (±0.015)	0.438 ± 0.038 (±0.016)	0.070 ± 0.023 (±0.025)	0.146 ± 0.030 (±0.016)
2f	Flat prior	1.57 ± 0.08 (±0.007)	0.464 ± 0.039 (±0.024)	0.439 ± 0.029 (±0.026)	0.075 ± 0.030 (±0.039)	0.137 ± 0.040 (±0.027)
1xwbi	Omit WBI	1.48 ± 0.10 (±0.004)	0.470 ± 0.036 (±0.016)	0.441 ± 0.034 (±0.017)	0.087 ± 0.025 (±0.026)	0.173 ± 0.034 (±0.017)
Standard Prior		1.68	0.517	0.462	0.177	0.273
EDGAR data set	V42_FT2010 Nonagricultural = industry + energy + transport + oil production + fossil fuel fires					
Nonagricultural		0.25	0.072	0.078	0.009	0.021
Total		0.89	0.296	0.298	0.077	0.148
Fertilizer data set	Applied N Fertilizers (TgN/yr), bold = www.sage.wisc.edu, plain text = Potter et al. (2010)					
Synthetic		12.9–**14.8**	5.8–**6.3**	6.0–**6.7**	**1.8**–2.1	**3.7**–3.9
Manure		16.9	4.8	5.0	0.8	2.3
Total N applied		28.8–30.6	10.6–11.1	11.0–11.7	2.6–2.9	6.0–6.2
Implied N_2O yield (%)		N/A	4.2–4.6%	3.7–4.2%	2.4–3.7%	2.2–3.0%
Yield (%) corrected for EDGAR nonagricultural sources		N/A	3.6–3.9%	3.1–3.5%	2.1–3.4%	1.9–2.7%

Note. For each of the cases, the reported uncertainty in the regionally integrated N_2O fluxes reflects the standard deviation over 2008–2014. Also reported in parentheses is the random uncertainty, estimated by computing a regionally aggregated posterior flux covariance matrix and taking the root mean square of the variance over each of the seven simulation years for each case.
[a]Estimated uncertainty due to a systematic error of ± 0.1 ppb in the background value. The estimate is based on the percentage change in the regionally aggregated flux, extrapolated to the total annual mean flux, in the summer 2010 sensitivity tests described in the supporting information.

several key sites were not established until mid-2007 or later (Table 1). We first examined the correlations between the NARR variables and the posterior N_2O flux on an individual monthly basis, that is, plotting the monthly mean N_2O flux from the Midwestern Corn/Soybean Belt for each of January, February, … December, against the corresponding monthly mean NARR variable for each year. We also examined correlations between the N_2O flux, integrated over longer periods ranging from seasonal to annual for each of 2007–2015, and the corresponding integral for the suite of NARR variables from those years.

We further used the regional monthly mean soil temperature NARR integrals to estimate when soil temperatures rose above 0°C in late winter/early spring and dropped below 10°C in fall. (The 10°C threshold corresponds to the likely timing of fall fertilizer application, while the potential significance of the 0°C crossing to soil N_2O production is described below.) These crossing dates were estimated to the nearest day based on a harmonic fit through each 13 month annual cycle of soil temperature (extending back 1 month to include the previous December). Because the Midwestern Corn/Soybean Belt extended widely across 11° of latitude, we identified 0°C and 10°C crossing days separately for several smaller-latitude bands within the belt, focusing on the central belt (38° to 43°N) where the most intensive cultivation and fertilizer use occurs (Figures 1 and 2).

3. Results

3.1. Excursions in Atmospheric N_2O From Background

Atmospheric N_2O is routinely enhanced by 2–3 ppb above the background value at many sites in the continental United States near agricultural areas, including WGC, LEF, and WKT (Figure 3). In contrast, at sites like THD on the Northern California coast, AMT on the northeastern U.S. coast, and others in western Canada and Alaska, observed N_2O generally lies within or only slightly above the ~0.2 ppb background value uncertainty, such that the signal to noise is relatively small over much of the model domain. Some of the largest excursions occur at station WBI in the heart of the Midwestern Corn/Soybean Belt, where observed atmospheric

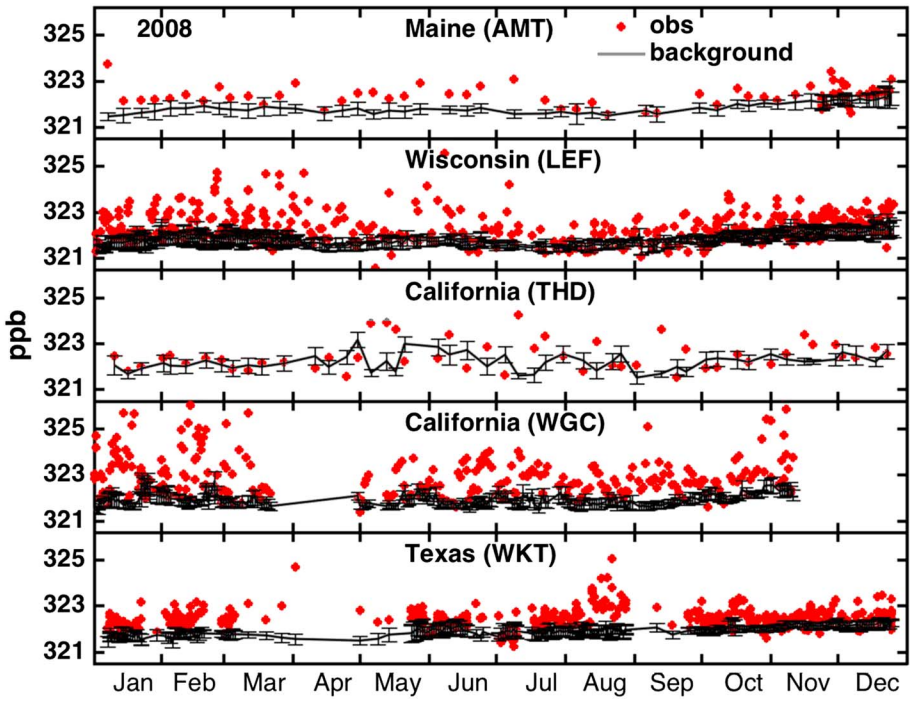

Figure 3. N_2O observations (red circles) over an annual cycle in 2008 at five selected surface sites. The gray line and error bars show the background value and its estimated uncertainty.

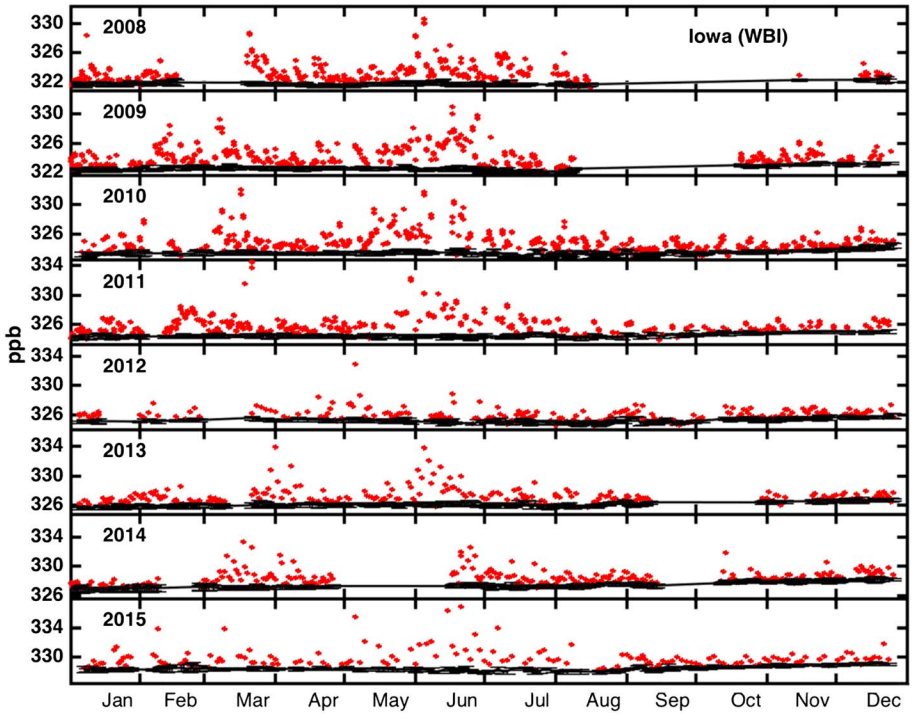

Figure 4. N_2O observations from West Branch, Iowa (WBI), showing interannual variability over 2008–2015. The gray line shows the background value and error bars (which are small compared to the large excursions from background). Note that all panels have the same *Y* axis span of 12 ppb, but the absolute values are incremented by 0.8 ppb/yr to accommodate the growth in atmospheric N_2O.

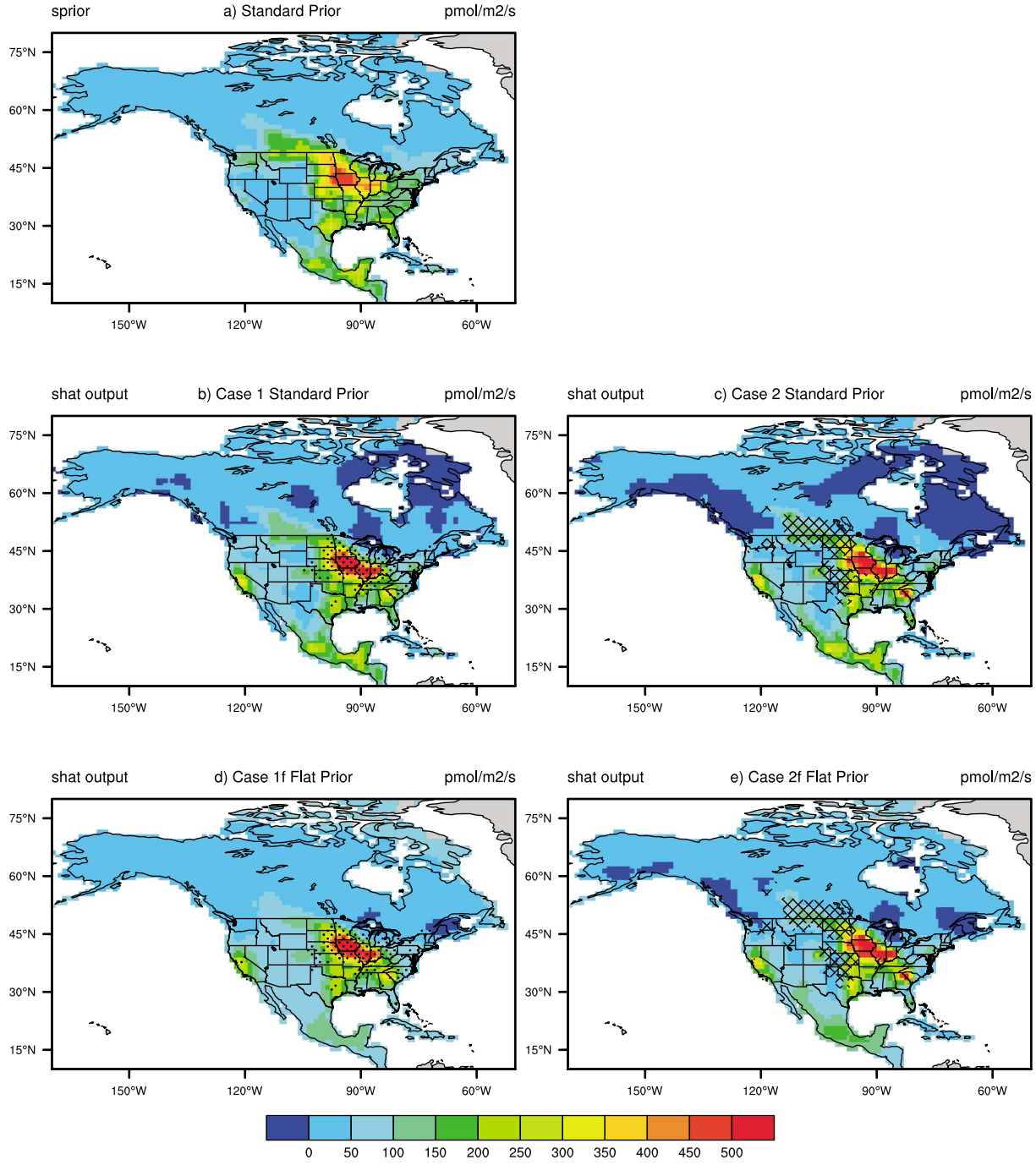

Figure 5. Top panel shows standard prior N_2O flux based on the posterior flux from the global atmospheric inversion of Saikawa et al. (2014). Remaining panels show 2008–2014 mean posterior N_2O emissions for Case 1 and Case 2 using the standard prior (middle row) and the flat prior (bottom row), respectively. Stippling shows areas in which more than 5% of the land is planted in wheat (cross hatching) or corn/soybean (dots).

N_2O routinely exceeds the background value by >10 ppb in springtime. These large excursions often have two separate peaks, with the first typically occurring around March and the second, generally larger, peak typically occurring around May/June (Figure 4).

3.2. Overview of Posterior Emissions: Magnitude and Spatial Distribution

The posterior flux $\hat{\mathbf{s}}$ consistently places the maximum N_2O flux in the Midwestern Corn/Soybean Belt across all years of the inversion (Figure 5). The results are relatively consistent between the Case 1 and Case 2

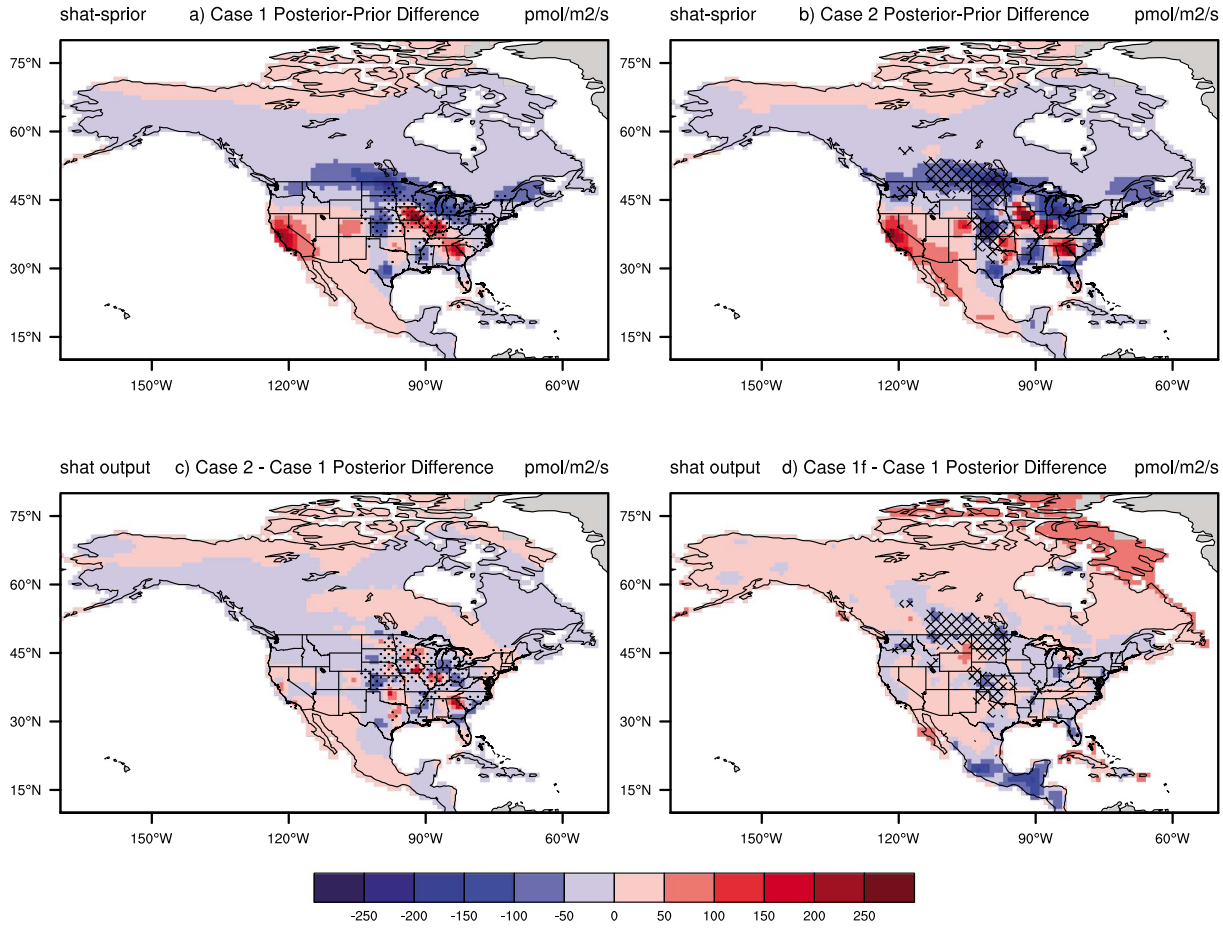

Figure 6. Comparison of selected inversion results with prior and with each other. All results reflect the mean of the 2008–2014 inversions. Top row: posterior-prior difference, for (a) Case 1 and (b) Case 2. Bottom row: (a) Case 2-Case 1 posterior difference and (b) Case1f-Case 1 posterior difference. Stippling shows areas in which more than 5% of the land is planted in wheat (cross hatching) or corn/soybean (dots).

covariance parameter choices and across the standard and flat priors (Figures 5 and 6). The inversion predicts substantially enhanced fluxes from California relative to the standard prior but substantially reduced fluxes across the north central United States and southern Canada, including the Northern Wheat Belt (Figures 5 and 6).

The total N_2O flux from the CT-L domain (spanning the whole of the North American land area from 10° to 80°N) is 1.46 ± 0.08 to 1.70 ± 0.09 Tg N/yr, depending on the choice of prior and covariance parameters (Table 3). Most of the cases give a smaller total flux than the prior estimate of 1.68 Tg N/yr, but much of the difference derives from modestly reduced (and occasionally negative) fluxes across the large land area of northern and eastern Canada (Figure 6). There are no NOAA sites in that region (Figure 1), and the reduction in uncertainty afforded by the inversion at the model grid scale is only on the order of 10–20% or less (Figure 7). The same is true of Central America, where only one site, MEX, is available. The greatest reduction in uncertainty, of up to 50% or better, occurs across a large area of the Midwestern Corn/Soybean Belt, as well as in the vicinity of well-sampled regions in California, Texas, Colorado, and the Southeast (Figure 7). In the Midwestern Corn/Soybean Belt, the posterior flux estimate of 0.46–0.49 Tg N/yr is slightly smaller than the prior estimate of 0.52 Tg N/yr (Table 1). In California, where the uncertainty reduction is comparable to the Midwest over much of the state, the statewide flux of 0.05–0.07 Tg N/yr is about 4 times larger than the prior estimate of 0.016 Tg N/yr. In contrast, the posterior flux from the Northern Wheat Belt, 0.07–0.1 Tg N/yr, is only about half that of the standard prior flux of 0.18 Tg N/yr. However, the collective uncertainties are relatively high from the Northern Wheat Belt (Table 3) and the uncertainty reduction is only in the range of 20–40%. When station WBI is removed from the inversion, the Midwestern Corn/Soybean Belt flux

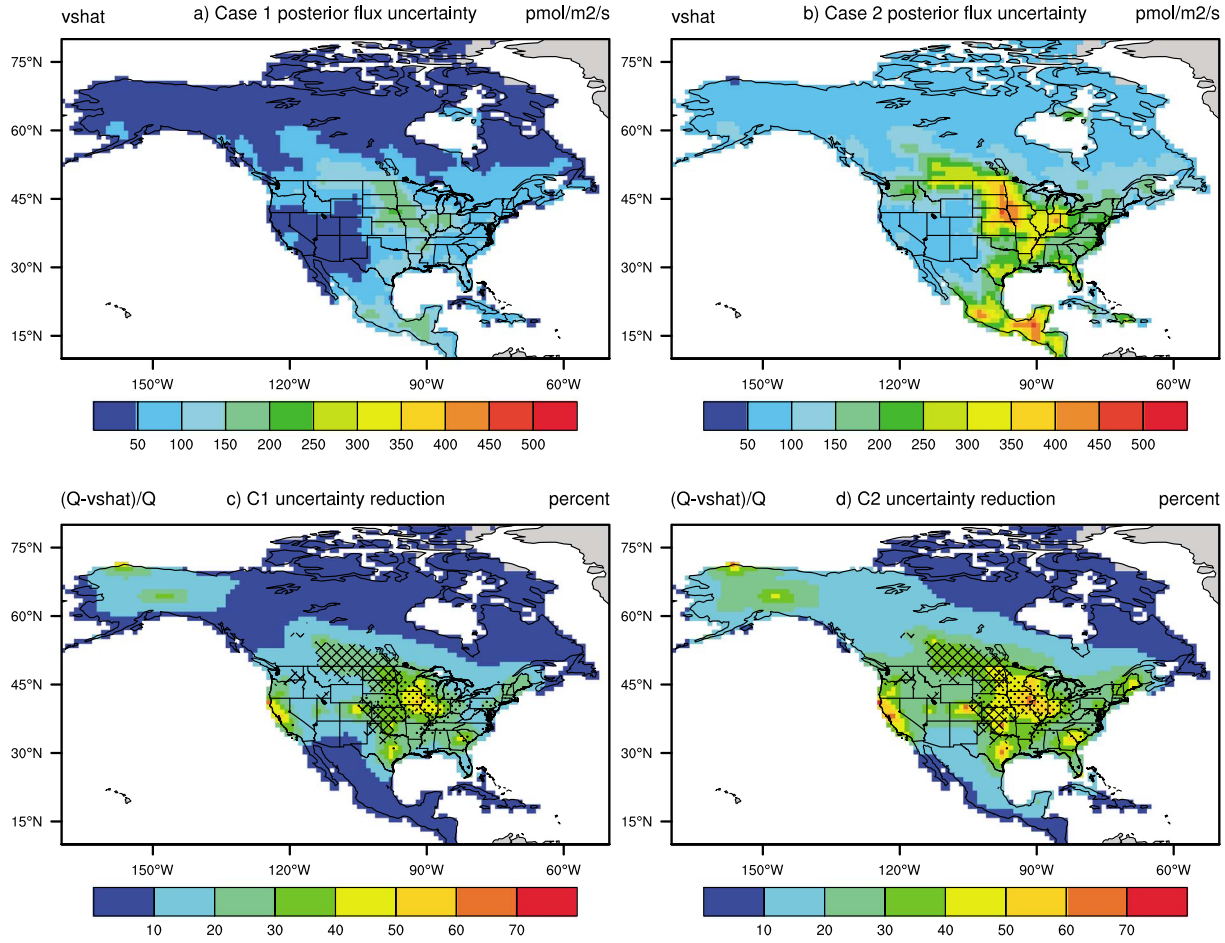

Figure 7. Top panels show the posterior flux uncertainty ($V\hat{s}$) for (a) Case 1 and (b) Case 2. Bottom panels show the reduction in the N_2O flux uncertainty, estimated as $(Q_{sum} - V\hat{s})/Q_{sum}$, for (c) Case 1 and (d) Case 2. Stippling in the bottom row panels shows areas in which more than 5% of the land is planted in wheat (cross hatching) or corn/soybean (dots). All results reflect the mean of the 2008–2014 inversions.

decreases by 0.02 Tg N/yr but remains the clear hot spot of emissions. The Northern Wheat Belt flux also decreases by 0.01 Tg N/yr.

A plot of the posterior mole fractions $\mathbf{H\hat{s}}$ versus the observed-minus-background mole fractions **z** shows substantial improvement over a similar plot of the prior mole fractions $\mathbf{Hs_p}$ versus **z** (Figure 8). The Case 2 parameters (representing looser prior/tighter model-data mismatch) yield larger correlation slopes (0.80 versus 0.73 for Case 1) and correlation coefficients ($R = 0.87$ versus 0.80 for Case 1), while results for the standard and flat priors for each case are generally similar.

3.3. Estimated N_2O Yield of Agricultural N Inputs

We estimated the N_2O yield associated with N fertilizer by dividing the annual mean posterior N_2O flux, integrated over the agricultural regions of interest defined in section 2.6, by the annual mean total N fertilizer application to those regions. The resulting quotient had considerable uncertainty, due both to uncertainty in the annual mean posterior N_2O flux and in the total synthetic plus organic N fertilizer input itself. The calculation suggested an N_2O yield of total applied N fertilizer in the range of 4.2 to 4.6% from the Midwestern Corn/Soybean Belt and 2.4–3.7% from the Northern Wheat Belt, which reduced to 3.6–3.9% and 2.1–3.4%, respectively, after subtracting estimated EDGAR industrial and other nonagricultural sources from these regions. Similar, slightly smaller yields were estimated from the All Corn/Soybean and All Wheat regions for these respective crops (Table 3).

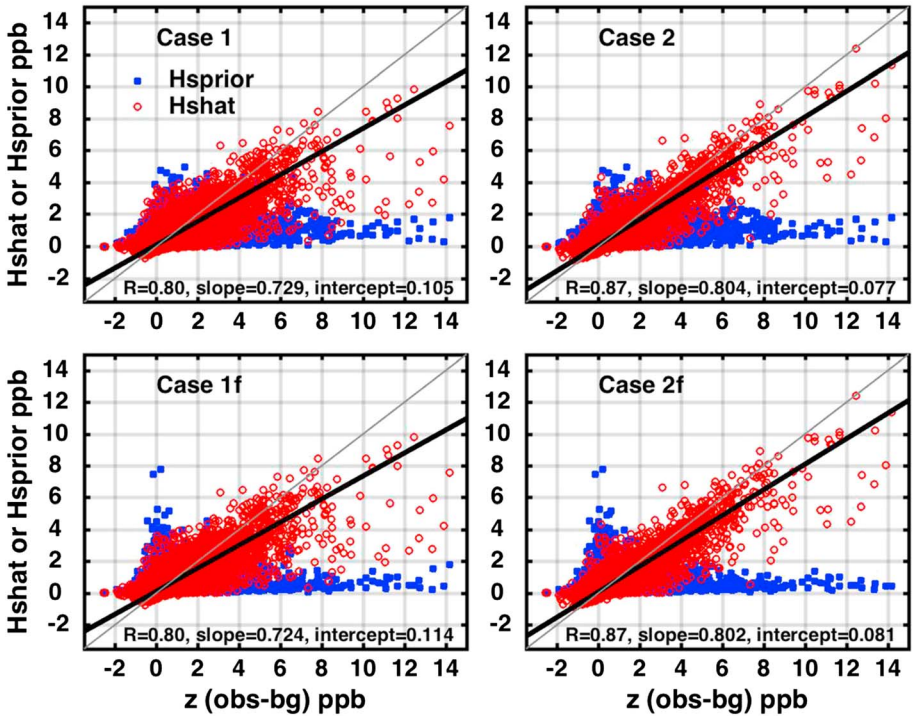

Figure 8. Posterior mole fractions $\mathbf{H\hat{s}}$ (red circles) and prior mole fractions $\mathbf{Hs_p}$ (blue squares) plotted against the observed-minus-background mole fractions **z** for each of the four cases, spanning all data used in the inversion from 2008 to 2014. For each case, the correlation coefficient and geometric mean regression slope and intercept are listed for $\mathbf{H\hat{s}}$ versus **z**. The 1:1 line is shown in light gray.

3.4. Seasonality of Posterior Emissions Over Selected Crop Regions

The daily posterior flux, integrated over the Midwestern Corn/Soybean region, shows considerable seasonal and interannual variability (Figure 9). While the seasonality differs from year to year, the results typically show dual maxima centered around springtime, with flatter emissions throughout the rest of the year. The first maximum is somewhat inconsistent year to year but tends to occur in February–March, around the time of the 0°C mean soil temperature crossing. The second maximum is larger and more sustained than the early spring maximum and occurs consistently in May/June. The prior flux, in contrast, varies little over an annual cycle, suggesting that the seasonality of the posterior fluxes derives more or less entirely from the inversion. As discussed in section 3.2, the annual mean magnitudes of the posterior and prior fluxes are in good agreement. However, viewed over an annual cycle, the posterior flux exceeds the prior by a factor of 2 to 3 during the spring and early summer peaks but drops well below the prior flux during the lows in late summer, fall, and winter. Among the posterior cases, the difference between covariance parameters in Case 1 versus Case 2 has the largest influence on the results, with more high-frequency variability in the Case 2 results but otherwise generally consistent overall seasonal patterns. There is no easily discernible difference between the standard versus flat prior cases in the Midwest but excluding data from WBI leads to clear reductions in most of the spring/early summer peaks.

Compared to Figure 9, the posterior N_2O flux integrated over the Northern Wheat region is relatively flat, seasonally less distinct, and shows more interannual variability (Figure 10). The pronounced May/June peak seen in the corn/soybean belt is largely missing, except in 2011. In most years, the largest and most distinct peak occurs in early spring in March or April, around the time of the 0°C mean soil temperature crossing. In contrast to the corn/soybean belt results, the posterior flux in the Northern Wheat Belt generally falls well below the prior flux, with only a few exceptions, mainly during spring. The integrated flux sometimes drops to or even below 0, especially during summer and for Case 2, reflecting occasional negative emissions predicted by the inversion (see section 4.5.2 for further discussion).

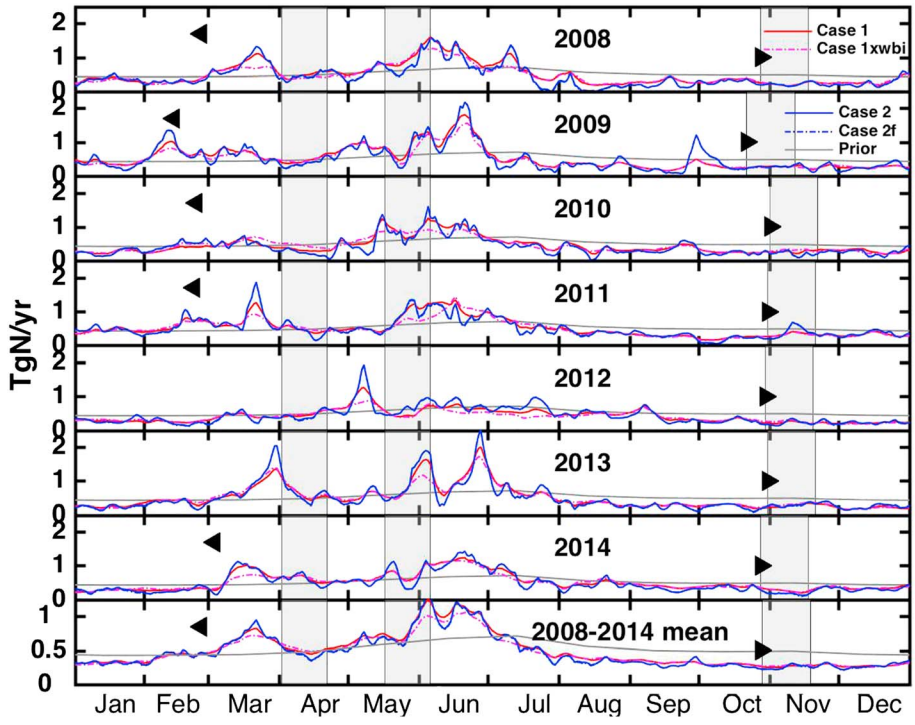

Figure 9. Posterior N_2O flux integrated over the Midwestern Corn/Soybean Belt (36° to 47°N, 102° to 80°W). Cases 1 (red) and 2 (blue) are defined based on the covariance parameters in Table 2 and use the standard prior derived from Saikawa et al. (2014), while Case 2f (blue dash) uses a flat prior. Case 1f is similar to Case 1 and therefore not shown. The magenta dashed line shows Case 1xwbi, in which N_2O data from WBI were omitted from the inversion. Left and right facing triangles show the approximate day when soil temperature climbs above 0°C and drops below 10°C (50°F), respectively. These triangles reflect mean soil temperature integrated over the central (38° to 43°N) latitude zone of the Midwestern Corn/Soybean Belt. In 2012 and 2013, no 0°C crossing symbol is plotted because the mean soil temperature remained above freezing. The bottom panel shows the mean seasonal cycle over 2008–2014. For better legibility, the *Y* axis scale is reduced by a factor of 2 relative to the individual year panels. Gray bands show rough estimates of the timing of the spring preplant, sidedress, and fall fertilizer applications.

3.5. Interannual Variability in Emissions

We conducted an analysis of interannual variability in N_2O emissions by comparing the integrated posterior fluxes to a suite of meteorological variables from NARR. This analysis focused on the Midwestern Corn/Soybean Belt, where we had the highest confidence in the inversion results. On an individual or bimonthly basis, the analysis yielded a positive correlation with precipitation in June and across May–June (R = .72) but a negative correlation with soil temperature in May–June (R = 0.71) as well as in March (R = 0.76). Soil moisture was negatively correlated with N_2O emissions in August (R = 0.83). When integrated annually, precipitation was weakly correlated to the posterior N_2O flux, soil temperature was weakly anticorrelated, and soil moisture was uncorrelated (Figure 11).

4. Discussion

4.1. Overview

The CT-L regional inversion estimates total N_2O emissions from North American land of about 1.6 ± 0.3 Tg N/yr, consistent with previous global atmospheric inversions and bottom-up inventories (Thompson et al., 2014). This total is smaller than the estimate of 2.1–2.6 Tg N/yr from the regional inversion of Miller et al. (2012), but much of the apparent difference derives from relatively small, uncertain fluxes over a large area of the domain, for example, Northern Canada, which was poorly resolved in both studies. Given the total global N_2O source of about 18 Tg N/yr (Ciais et al., 2013), the total flux of 1.6 ± 0.3 Tg N/yr suggests that North America is a modest term in the global budget, accounting for about 9% of total global emissions.

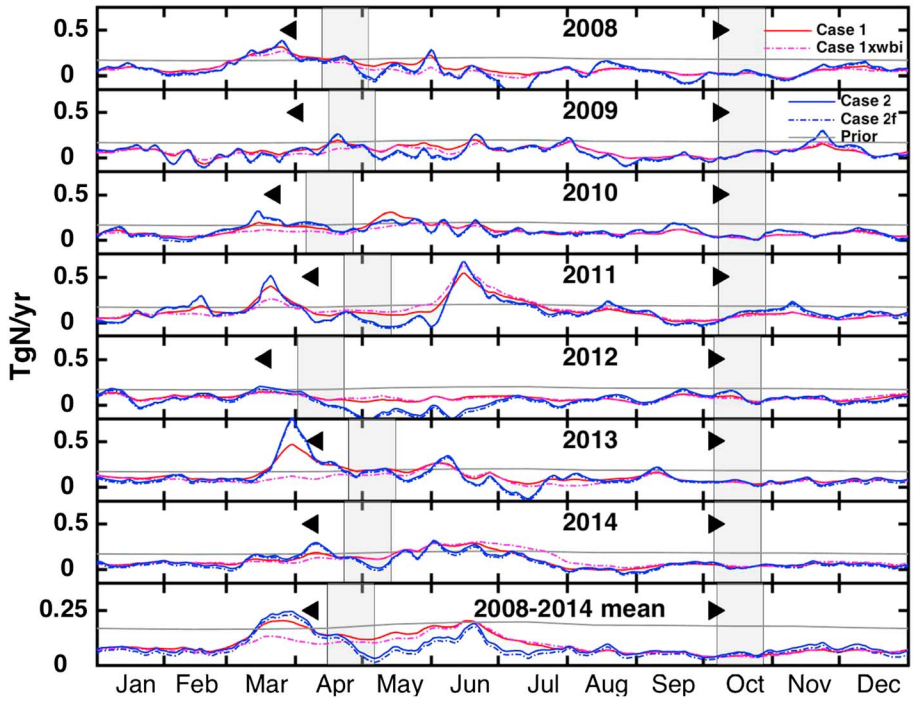

Figure 10. Same as Figure 9 but showing the posterior N_2O flux integrated over the Northern Wheat Belt (47°N to 54°N, 115° to 95°W). Left and right facing triangles show the approximate day when mean soil temperature across the belt climbs above 0°C and drops below 10°C (50°F), respectively. Gray bands show rough estimates of the timing of the spring preplant and fall fertilizer applications, which are assumed to vary year to year according to soil temperature.

The inversion identifies a clear hot spot for N_2O emissions in the heart of the U.S. Midwestern Corn/Soybean Belt. The total N_2O source from this belt is approximately 0.46–0.49 Tg N/yr or ~30% of total North American N_2O emissions. Subtracting the EDGAR industrial and energy-related sources (0.072 Tg N/yr) suggests a mainly agricultural source from the region of 0.39–0.42 Tg N/yr. An alternative analysis, in which the corn/soybean source region is defined based on a minimum crop area threshold rather than latitude/longitude bounds, suggests a corn/soybean related N_2O source of 0.36–0.38 Tg N/yr.

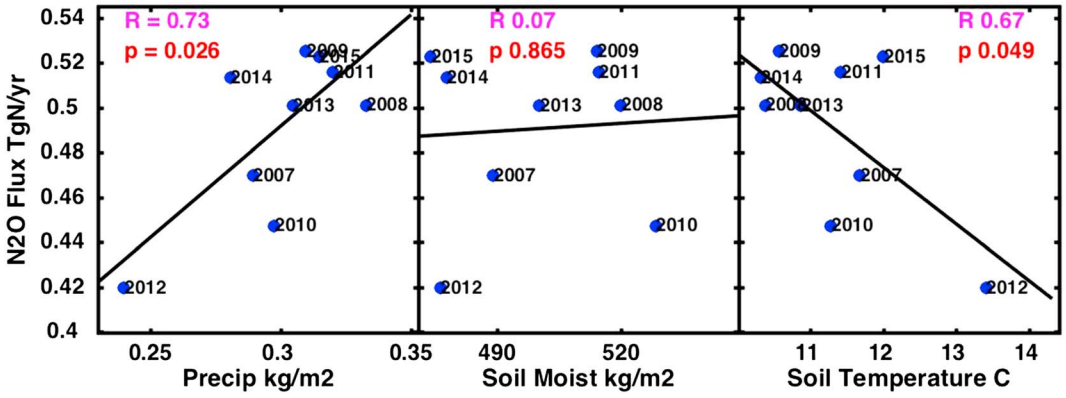

Figure 11. Posterior N_2O flux for Case 1 integrated over the Midwestern Corn/Soybean Belt (36°N to 47°N, 102° to 80°W) from 1 January to 31 December for each year from 2007 to 2015. N_2O fluxes are plotted as a function of mean (a) precipitation, (b) soil moisture, and (c) soil temperature from the North American Regional Reanalysis, averaged over the same region and time span. Black slope lines, correlation coefficients *R* and *p* values show results of least squares linear regression.

We note finally that our finding that the Midwestern Corn/Soybean Belt is a large source of N_2O can be considered in the context that approximately 40% of the U.S. corn crop in recent years has been used for purposes "other" than human food or livestock feed, that is, mainly for biofuel (FAO, 2016). Given N_2O's Global Warming Potential of 265 over 100 years relative to CO_2 (Myhre et al., 2013), the net greenhouse gas benefit, as seen from a carbon cycle perspective, may be negated when one factors in the enhanced N_2O production associated with biofuel crops like corn (Crutzen et al., 2008; Erisman et al., 2010). Assuming a Global Warming Potential of 265, our estimated N_2O fluxes in Table 3 suggest emissions of 0.041–0.048 Pg C/yr CO_2-equivalent associated with corn/soybean agriculture. In general, the large N_2O emissions from the corn/soybean belt raise policy questions that merit further exploration but are beyond the scope of this paper.

4.2. Comparison to EDGAR Inventory

Several previous regional inversions over North America have suggested that the EDGAR inventory might underestimate U.S. Midwestern N_2O emissions by a factor of ~3 (Kort et al., 2008, 2010; Miller et al., 2012). This finding generally is not supported by our results, which extend over a longer time scale and are constrained by a more comprehensive network of measurements than previous results. The EDGAR inventory is an annual mean anthropogenic flux that is not resolved seasonally. Our results suggest that EDGAR indeed underestimates N_2O emissions in spring and early summer, by a factor of 3 in the corn/soybean belt, but this is balanced by EDGAR's tendency to overestimate N_2O during other seasons of the year. Indeed, some of the previous inversions have noted that a better understanding of seasonality might explain the apparent discrepancy between their results and EDGAR.

The idea of threefold underestimate by EDGAR was never plausible from a global budget perspective, since a number of constraints argue against such large fluxes out of North America. First, the total anthropogenic source is relatively well known at about 6–7 Tg N/yr, based on the observed growth rate and total burden of atmospheric N_2O and its stratospheric loss rate (Hirsch et al., 2006; Prather et al., 2015) for contemporary and preindustrial atmospheres. Thus, the total global EDGAR v4.2 source (6.7 Tg N/yr) is about right, such that if EDGAR is truly underestimating North American emissions by a factor of 3, it must be substantially overestimating them elsewhere in the world. This seems unlikely, given that the United States and Canada consume only 12–15% of global N fertilizers (FAO, 2016), which furthermore tend to be applied more efficiently, with lower leaching losses, than other countries like China (Ju et al., 2009; Vitousek et al., 2009). In addition, the fraction of N fertilizer emitted as N_2O is likely higher in tropical and subtropical areas than in the temperate United States (Bouwman et al., 2002).

Previous regional inversions focused specifically on California have suggested that the EDGAR inventory might underestimate that state's N_2O emissions by a factor of ~3–4 (Jeong et al., 2012; Xiang et al., 2013). Our results from California can be roughly compared to the previous N_2O inversion study by Xiang et al. (2013), which was performed at much higher spatial resolution (4 km), but over a considerably shorter (May–June 2010) time period using data from the CalNex aircraft campaign. They estimated a total statewide N_2O flux of 0.0155–0.0170 Tg N over those two months, which they extrapolated to an annual flux of 0.042 ± 0.011 Tg N/yr. We estimate a similar May–June 2010 flux of 0.0147–0.0154 Tg N and a 2008–2014 flux ranging from 0.045 to 0.070 Tg N/yr. These fluxes, like those of Xiang et al. (2013), are a factor of 3–4 larger than our prior EDGAR-based estimate. However, our California results stand in contrast to our Midwestern and nationwide results, which are generally consistent with EDGAR on an annual mean basis. It is notable that our nationwide results are not strongly leveraged by California N_2O emissions, which account for only 3–4% of our estimated North American total. We note also that the ratio of manure:synthetic N fertilizer input to California (3.1) is relatively large compared to most Midwestern states, for example, 0.8 in Iowa and 0.3 in Illinois (calculations based on Potter et al., 2010). This suggests the possibility that EDGAR may underestimate manure-related N_2O emissions, which are calculated using a particularly complex algorithm (IPCC, 2006).

4.3. Seasonality, Fertilizer Timing, and Emission Fraction

The inversion identifies strong seasonality in Midwestern Corn/Soybean N_2O emissions, which are elevated in spring and early summer, with a double peak structure (except in 2012), relative to the rest of the year (Figure 9). The smaller February–March maximum occurs somewhat early to be a fertilizer peak and rather may reflect a microbial N_2O pulse associated with freeze-thaw soil dynamics in late winter/early spring

(Wagner-Riddle et al., 2017).The fact that the February–March peak tends to occur around the time of the 0°C mean soil temperature crossing in the corn/soybean belt lends support to this explanation, as does the fact that the peak is largely absent in 2012 and 2013, which were warm winters in which soils in much of the southern part of the corn/soybean belt never froze.

The second maximum predicted by the inversion typically begins in April, builds to a peak in May–June, and extends in some years well into July. This timing of this broad maximum appears to correspond to the early preplant and late spring "sidedress" fertilizer applications to the Midwestern corn crop described in section 2.6.2. The April–July N_2O flux is substantially stronger than the February–March flux in all years, with those two periods contributing 50 ± 3% and 18 ± 2%, respectively, of total annual emissions across 2008–2014.

There are few quantitative data on the relative amounts of the preplant, sidedress, and late fall fertilizer applications. A recent global synthetic fertilizer data set assumes proportions of 70% preplant and 30% sidedress (assumed to occur 45 days after the preplant application) (Nishina et al., 2017), but communications from agricultural university extension offices suggest that a large fraction of the annual total N fertilizer, including manure and synthetic anhydrous ammonia, is applied in late fall. Interestingly, there is no obvious signature in the inversion results of this late fall application (Figure 9). Overall, the inversion results suggest that the 6 month span from February–July accounts for two thirds of total annual emissions in the corn/soybean belt and that microbial N_2O production is influenced by both N fertilizer inputs and climate.

N_2O emissions from the Northern Wheat Belt differ substantially in their seasonality from the Midwestern Corn/Soybean Belt, most notably in the lack of a clear May/June peak in most years (Figure 10). In many years, there is evidence in Figure 10 of an early spring pulse, which does not appear obviously linked to the main spring fertilizer application in the Northern Wheat Belt, although the timing of the latter is poorly known. Alternatively, the early spring pulse could reflect freeze-thaw dynamics, since it tends to occur around the time of the 0°C mean soil temperature crossing in the Northern Wheat Belt (Wagner-Riddle et al., 2017). However, the reduction in the Northern Wheat flux in the Case 1xwbi simulations suggests that the early spring pulse is driven in part by N_2O observations at WBI, which sits in the Midwestern Corn/Soybean Belt (Figure 9). In general, inversion uncertainty in the Northern Wheat Belt is large, as discussed below.

The estimated annual mean fraction of total synthetic plus organic N fertilizer emitted as N_2O is generally larger from the Midwestern Corn/Soybean Belt (3.6–3.9%) than from the Northern Wheat Belt (2.1–3.4%) (Table 3). For comparison, the 2 to 2.5% yield estimated by Davidson (2009), based on global box model calculations, is consistent with our estimated Northern Wheat fraction but is low relative to the Midwestern Corn/Soybean fraction. The different yields could reflect the typical lack of a May/June fertilizer application in the Northern Wheat Belt, which avoids an N input during temperature and soil moisture conditions that may be conducive to largest N_2O losses. Alternatively, the high apparent yield from the Midwestern Corn/Soybean region may neglect the influence of additional N inputs from biological N_2 fixation by soybeans. Assuming a typical N_2 fixation rate of 62 kg N/ha (Vitousek et al., 2009), the 114 million ha area of soybean in the Midwest Corn/Soybean Belt (FAO, 2016) fixes approximately 7 Tg N/yr. This suggests a total fertilizer + biological fixation N input to the region of 17.6–18.1 Tg N/yr (Table 3), corresponding to an N_2O yield of 2.2–2.4%.

4.4. Interannual Variability

The N_2O emissions estimated by the inversion in the Midwestern Corn/Soybean Belt are consistently elevated in spring and early summer, but there is substantial interannual variability in their timing and magnitude. This suggests a link to climate, which can affect the timing of N_2O emissions in at least two ways: directly by driving spikes in soil moisture or temperature that lead to a burst of microbial N cycling activity and more indirectly by influencing the timing of fertilizer application itself. The latter issue may be one reason that we found relatively few strong correlations between the posterior N_2O flux and climate-related parameters (soil temperature, precipitation, and soil moisture) when the N_2O fluxes were compared to these variables on a monthly basis.

Over longer annual time integrals, the posterior N_2O flux was positively correlated to precipitation and negatively correlated to soil temperature (Figure 11), suggesting that cooler years with higher rainfall tend to

produce higher N_2O emissions. Indeed, there is a strong basis in the literature for expecting microbial N_2O production to be influenced and enhanced by rainfall (Firestone & Davidson, 1989; Saikawa et al., 2013). However, warm climates are also generally thought to produce higher microbial activity and N_2O emissions (Bouwman et al., 1993; Parton et al., 2001). The anticorrelation between mean temperature and N_2O flux both in late spring and annually (Figure 11) is therefore somewhat puzzling but may reflect the fact that warm temperatures tend to dry out soils and that this effect dominates the correlation with temperature on an interannual basis. The mean seasonal pattern, with highest emissions in May/June (Figure 9), is still supportive of a positive influence of temperature on N_2O emissions on a seasonal basis.

It should be noted that the correlations in Figure 11 are relatively weak and sensitive to inclusion of 2012. This was an outlier drought year in the Midwest, when N_2O emissions from the corn/soybean belt were substantially lower than in other years (0.42 Tg N/yr versus the 2008–2014 mean of 0.49 Tg N/yr for Case 1). Thus, future study and inclusion of additional years are needed for more confidence that the N_2O flux is robustly correlated to these climate variables.

We note finally that, while the CT-L methodology is capable of detecting secular trends in emissions (Hu et al., 2015), our results suggest that interannual variability likely dominates any such trend in North American emissions. This finding is not surprising given that N fertilizer use, a principal driver of increasing emissions, was relatively stable in North America over 2008–2014 (FAO, 2016). In contrast, global inversions have detected increasing trends in N_2O emissions from eastern and southern Asia, where most of the new growth in N fertilizer use is occurring (Thompson et al., 2014).

4.5. Inversion Uncertainties

4.5.1. Background Values

Excursions above background are critical to the inversion, since the vector **z** in equation (1) is not the atmospheric N_2O observation itself but rather the difference between that observation and a prescribed background value. At a number of stations, especially in Canada, Alaska, and the eastern United States, the excursions in N_2O generally fall close to the background value, such that the inversion cannot easily distinguish the magnitude or even the sign of the net flux from a large part of the domain. This raises concerns that the inversion may be influenced disproportionately by sites, such as WBI, where excursions in observed N_2O routinely rise above the background noise. On the other hand, the fact that many sites do not show large enhancements above background is a valid constraint, especially at sites (e.g., AMT, Table 1) with a large number of samples.

Although at 0.2 ppb the mean estimated uncertainty in our background values is relatively small, we performed a set of sensitivity tests examining the impact of random and systematic uncertainty. In general, we found that the addition of random uncertainty to the background values led to only small changes in our integrated regional results, on the order of a few percent or less. In contrast, systematic shifts of ±0.1 ppb led to ±20%, 5%, and 30% changes in the predicted fluxes from North America, the Midwestern Corn/Soybean Belt, and the Northern Wheat Belt, respectively (supporting information Figures S1–S3). These uncertainties are presented in Table 3 and suggest that systematic error in the background represents a relatively large uncertainty, particularly in the Northern Wheat Belt, compared to the other sources of uncertainty quantified in our analysis. In a related set of sensitivity tests, we found that adjusting the individual elements σ_r^2 of the **R** vector according to the background uncertainty of each N_2O measurement led to small changes of 1–2% or less for all of North America and the Midwestern Corn/Soybean Belt and changes of up to 9% in the Northern Wheat Belt (supporting information Figures S4–S6).

4.5.2. Negative Fluxes

The inversion predicts occasional negative N_2O fluxes throughout most of the CT-L domain, with the exception of California and the Midwest and central United States. However, the net flux integrated over a seasonal or annual period is negative in a much more limited part of the domain, mainly in areas of Canada outside of the Northern Wheat Belt (Figure 5). While soil uptake of N_2O has been observed in some field studies, it is a small term (only −0.01 Tg N/yr) in the IPCC global budget, with an order of magnitude uncertainty (Ciais et al., 2013). The negative fluxes predicted by the inversion therefore are probably not realistic.

Previous inversion studies have used a range of strategies to prevent unrealistic negative fluxes, including lognormal data transformations, Lagrange multipliers, and Markov chain Monte Carlo methods (Ganesan

et al., 2014; Miller et al., 2014). We experimented here with a nonnegativity enforcement algorithm that started with the standard posterior solution but then iteratively corrected the whole field for negative fluxes using Lagrange multipliers and the bounded, limited-memory Broyden-Fletcher-Goldfarb-Shanno approach (Byrd et al., 1995). In principle, the iterative solution should have conserved mass, with any removal of negative fluxes accompanied by weaker positive fluxes elsewhere (Miller et al., 2014). In practice, the nonnegativity algorithm was very slow to converge and led to an overall net increase in N_2O emissions of about 0.3–0.4 Tg N/yr over the CT-L domain. This was due to an overall increase throughout Canada, with particularly strong enhancement in Ontario, east of the Northern Wheat Belt, which was only partially offset by small decreases in the Midwestern Corn/Soybean Belt. The nonnegativity algorithm is not included in the results presented in Table 3, due to concerns over mass conservation and the lack of adequate constraints in northern and eastern Canada, but is an issue that will be addressed in future development of CT-L.

4.5.3. Sensitivity to WBI

WBI in West Branch, Iowa, lies in the heart of the Midwestern Corn/Soybean Belt. This site consistently displays some of the highest observed excursions in atmospheric N_2O above background, of up to 10–12 ppb or higher, especially in spring and early summer. The selective removal of WBI tower and aircraft data from the inversion (Case 1xwbi) not surprisingly leads to a small ~3% overall decrease in the total North American flux with most of the reduction coming from the Midwestern Corn/Soybean Belt and much of the remainder coming from the Northern Wheat Belt. The spring/early summer maxima in the N_2O fluxes from the Midwestern Corn/Soybean Belt are reduced in magnitude but not fundamentally changed in timing or character (Figure 9). The removal of WBI has a more mixed effect on the structure of the Northern Wheat Belt fluxes, more or less entirely removing the large early spring peak in 2013, but enhancing the June peak predicted in 2011 (Figure 10). Overall, the results of Case 1xwbi suggest that the Midwestern Corn/Soybean Belt's role as the hot spot of North American emissions is enhanced but not dependent on WBI; that is, the broader network of stations surrounding the Midwest supports a strong source from this region independent of WBI.

4.5.4. Covariance Parameters

We used the MLE method (Michalak et al., 2005) to select optimal parameters for the **R** and **Q** covariance matrices. The MLE method was applied to selected 3 month segments of data, corresponding to spring (April–June), summer (June–August), and fall (October–December). Longer periods of analysis were not computationally feasible. The summer MLE analysis resulted in a clear choice (i.e., an identifiable minimum in $L\theta$, defined as per Michalak et al., 2005) of l_τ = 35 days and l_s = 300 km for the temporal and spatial correlation lengths, respectively. Using those parameters in further MLE calculations, optimal values of σ_r^2 and $\boldsymbol{\sigma_s}$ were also identified, corresponding to Case 2 in Table 2. In contrast, when applied to spring or fall, there was no clear optimal value for l_τ or l_s. However, when those parameters were fixed at 35 days and 300 km, respectively, the MLE method applied to the spring months suggested the optimal values of σ_r^2 and $\boldsymbol{\sigma_s}$ listed for Case 1 in Table 2. Overall, while the MLE method provided useful guidance for the current study, alternative covariance parameter choices should be explored in future work.

5. Conclusions

The CT-L regional inversion predicts total North American nitrous oxide (N_2O) emissions of 1.6 ± 0.3 Tg N/yr over 2008–2013, with a clear emissions hot spot in the Midwestern Corn/Soybean Belt. The total N_2O source from this belt, defined from 36° to 47°N and 102° to 80°W, was estimated at 0.46 ± 0.49 Tg N/yr, more or less consistent with the EDGAR inventory, and accounting for 30% of total North American emissions. After correcting for EDGAR nonagricultural emissions, this N_2O flux is equivalent to 3.6–3.9% of the total synthetic plus organic N fertilizer applied to the crops within this region, although this yield fraction reduces to 2.2–2.4% if additional N inputs from N_2 fixation by soybeans are considered. In contrast, the N_2O flux estimated from the Northern Wheat Belt, at 0.07–0.1 Tg N/yr, was only about half of the EDGAR flux, with an estimated agricultural N_2O/total N fertilizer yield of 2.1–3.4%. These lower values could reflect the lack of N_2 fixing crops in the wheat region, the typical lack of fertilizer application in late spring/early summer (in contrast to corn/soybean crops), or the high uncertainty of the inversion in the Northern Wheat region. Future work to improve confidence in the inversion results should include expanding network coverage to northern and eastern Canada, estimating the background correction within the inversion rather than prescribing it, and exploring a wider variety of atmospheric transport models and covariance uncertainty parameters.

Acknowledgments
C. D. N. and E. S. acknowledge support from the NOAA Climate Program Office's AC4 program, award NA13OAR4310061 and NA13OAR4310059. C. D. N. thanks Lei Hu and many others from the weekly LPDM discussion group for their helpful comments on the results presented here. All authors are deeply grateful to the many people who have contributed to the production of the excellent N_2O data sets that have made this study possible. We thank Vineet Yadav and Sourish Basu for guidance on implementation of and modifications to the inversion framework and two anonymous reviewers for their helpful comments, which much improved the manuscript. The data used in this study can be obtained through the NOAA Global Monitoring Division at https://www.esrl.noaa.gov/gmd/dv/iadv/ or by contacting ed.dlugokencky@noaa.gov. The CarbonTracker-Lagrange inversion code is described at (www.esrl.noaa.gov/gmd/ccgg/carbontracker-lagrange/doc/) and can be obtained by contacting kirk.thoning@noaa.gov. N_2O inversion results can be obtained by contacting cynthia.nevison@colorado.edu.

References

Andrews, A. E., Kofler, J. D., Trudeau, M. E., Williams, J. C., Neff, D. H., Masarie, K. A., et al. (2014). CO_2, CO, and CH_4 measurements from tall towers in the NOAA Earth System Research Laboratory's Global Greenhouse Gas Reference Network: Instrumentation, uncertainty analysis, and recommendations for future high-accuracy greenhouse gas monitoring efforts. *Atmospheric Measurement Techniques*, *7*(2), 647–687. www.atmos-meas-tech.net/7/647/2014/doi:10.5194/amt-7-647-2014

Bouwman, A. F., Fung, I., Matthews, E., & John, J. (1993). Global analysis of the potential for N_2O production in natural soils. *Global Biogeochemical Cycles*, *7*(3), 557–597. https://doi.org/10.1029/93GB01186

Bouwman, A. F., van der Hoek, K. W., & Olivier, J. G. J. (1995). Uncertainties in the global source distribution of nitrous oxide. *Journal of Geophysical Research*, *100*(D2), 2785–2800. https://doi.org/10.1029/94JD02946

Bouwman, A. F., Boumans, L. J. M., & Batjes, N. H. (2002). Estimation of global NH_3 volatilization loss from synthetic fertilizers and animal manure applied to arable lands and grasslands. *Global Biogeochemical Cycles*, *16*(2), 1024. https://doi.org/10.1029/2000GB001389

Byrd, R., Lu, P., Nocedal, J., & Zhu, C. (1995). A limited memory algorithm for bound constrained optimization. *SIAM Journal on Scientific Computing*, *16*(5), 1190–1208. https://doi.org/10.1137/0916069

Chen, Z., Griffis, T. J., Millet, D. B., Wood, J., Lee, X., Baker, J. M., et al. (2016). Partitioning N_2O emissions within the US Corn Belt using an inverse modeling approach. *Global Biogeochemical Cycles*, *30*, 1192–1205. https://doi.org/10.1002/2015GB005313

Ciais, P., Sabine, C., Bala, G., Bopp, L., Brovkin, V., Canadell, J., et al. (2013). Carbon and other biogeochemical cycles. In T. F. Stocker, et al. (Eds.), *Climate change 2013: The Physical Science Basis. Contribution of Working Group I to the Fifth Assessment Report of the Intergovernmental Panel on Climate Change* (Chap. 6, pp. 465–570). Cambridge, United Kingdom and New York: Cambridge University Press.

Corazza, M., Bergamaschi, P., Vermeulen, A. T., Aalto, T., Haszpra, L., Meinhardt, F., et al. (2011). Inverse modelling of European N2O emissions: Assimilating observations from different networks. *Atmospheric Chemistry and Physics*, *11*, 2381–2398. https://doi.org/10.5194/acp-11-2381-2011

Crutzen, P. J. (1974). Estimates of possible variations in total ozone due to natural causes and human activities. *Ambio*, *3*, 201–210.

Crutzen, P. J. (1976). Upper limits on atmospheric ozone reductions following increased application of fixed nitrogen to the soil. *Geophysical Research Letters*, *3*, 169–172.

Crutzen, P. J., Mosier, A. R., Smith, K. A., & Winiwarter, W. (2008). N_2O release from agro- biofuel production negates global warming reduction by replacing fossil fuels. *Atmospheric Chemistry and Physics*, *8*(2), 389–395. https://doi.org/10.5194/acp-8-389-2008

Davidson, E. A. (2009). The contribution of manure and fertilizer nitrogen to atmospheric nitrous oxide since 1860. *Nature Geoscience*, *2*(9), 659–662. https://doi.org/10.1038/ngeo608

Draxler, R. R., & Hess, G. D. (1998). An overview of the HYSPLIT_4 modeling system of trajectories, dispersion, and deposition. *Australian Meteorological Magazine*, *47*, 295–308.

EDGAR (2009). European Commission, Joint Research Centre (JRC)/Netherlands Environmental Assessment Agency (PBL): Emission Database for Global Atmospheric Research (EDGAR), release version 4.0. Retrieved from http://edgar.jrc.ec.europa.eu

Eichner, M. J. (1990). Nitrous oxide emissions from fertilized soils: Summary of available data. *Journal of Environmental Quality*, *19*, 272–280.

Erisman, J. W., van Grinsven, H., Leip, A., Mosier, A., & Bleeker, A. (2010). Nitrogen and biofuels; An overview of the current state of knowledge. *Nutrient Cycling in Agroecosystems*, *86*(2), 211–223. https://doi.org/10.1007/s10705-009-9285-4

Firestone, M. K., & Davidson, E. A. (1989). Microbiological basis of NO and N_2O production and consumption in soil. In M. O. Andreae & D. S. Schimel (Eds.), *Exchange of trace gases between terrestrial ecosystems and the atmosphere* (pp. 7–21). Chichester: Wiley.

Food and Agriculture Organization of the United Nations (FAO) (2016). *Production and trade statistics*. Rome: Food and Agric. Org. of the U. N. Retrieved from http://faostat.fao.org/

Francey, R. J., Steele, L. P., Spencer, D. A., Langenfelds, R. L., Law, R. M., Krummel, P. B., et al. (2003). The CSIRO (Australia) measurement of greenhouse gases in the global atmosphere. In N. W. Tindale, N. Derek, & P. J. Fraser (Eds.), *Baseline Atmospheric Program Australia 1999–2000* (pp. 42–53). Melbourne, Australia: Bureau of Meteorology and CSIRO Atmospheric Research.

Fu, C., Lee, X., Griffis, T. J., Dlugokencky, E. J., & Andrews, A. E. (2017). Investigation of the N_2O emission strength in the U.S. Corn Belt. *Atmospheric Research*, *194*, 66–77. https://doi.org/10.1016/j.atmosres.2017.04.027

Galloway, J. N., Dentener, F. J., Capone, D. G., Boyer, E. W., Howarth, R. W., Seitzinger, S. P., et al. (2004). Nitrogen cycles: past, present and future. *Biogeochemistry*, *70*(2), 153–226. https://doi.org/10.1007/s10533-004-0370-0

Ganesan, A. L., Manning, A. J., Grant, A., Young, D., Oram, D. E., Sturges, W. T., et al. (2015). Quantifying methane and nitrous oxide emissions from the UK and Ireland using a national-scale monitoring network. *Atmospheric Chemistry and Physics*, *15*(11), 6393–6406. https://doi.org/10.5194/acp-15-6393-2015

Ganesan, A. L., Rigby, M., Zammit-Mangion, A., Manning, A. J., Prinn, R. G., Fraser, P. J., et al. (2014). Characterization of uncertainties in atmospheric trace gas inversions using hierar- chical Bayesian methods. *Atmospheric Chemistry and Physics*, *14*, 3855–3864. https://doi.org/10.5194/acp-14-3855-2014

Gourdji, S. M., Mueller, K. L., Yadav, V., Huntzinger, D. N., Andrews, A. E., Trudeau, M., et al. (2012). North American CO_2 exchange: Inter-comparison of modeled estimates with results from a fine-scale atmospheric inversion. *Biogeosciences*, *9*(1), 457–475. https://doi.org/10.5194/bg-9-457-2012

Hall, B. D., Dutton, G. S., & Elkins, J. W. (2007). The NOAA nitrous oxide standard scale for atmospheric observations. *Journal of Geophysical Research*, *112*, D09305. https://doi.org/10.1029/2006JD007954

Hammerling, D. M., Michalak, A. M., & Kawa, S. R. (2012). Mapping of CO2 at high spatiotemporal resolution using satellite observations: Global distributions from OCO-2. *Journal of Geophysical Research*, *117*, D06306. https://doi.org/10.1029/2011JD017015

Hegarty, J., Draxler, R. R., Stein, A. F., Brioude, J., Mountain, M., Eluszkiewicz, J., et al. (2013). Evaluation of Lagrangian particle dispersion models with measurements from controlled tracer releases. *Journal of Applied Meteorology and Climatology*, *52*(12), 2623–2637. https://doi.org/10.1175/JAMC-D-13-0125.1

Hirsch, A. I., Michalak, A. M., Bruhwiler, L. M., Peters, W., Dlugokencky, E. J., & Tans, P. P. (2006). Inverse modeling estimates of the global nitrous oxide surface flux from 1998–2001. *Global Biogeochemical Cycles*, *20*, GB1008. https://doi.org/10.1029/2004GB002443

Hofmann, D. J., Butler, J. H., Dlugokencky, E. J., Elkins, J. W., Masarie, K., Montzka, S. A., & Tans, P. (2006). The role of carbon dioxide in climate forcing from 1979–2004: Introduction of the annual greenhouse gas index, *Tellus B*, *58B*, 614–619; for update, see: https://www.esrl.noaa.gov/gmd/aggi/aggi.html

Hu, L., Montzka, S. A., Miller, J. B., Andrews, A. E., Lehman, S. J., Miller, B. R., et al. (2015). U.S. emissions of HFC-134a derived for 2008–2012 from an extensive flask-air sampling network. *Journal of Geophysical Research: Atmospheres*, *120*, 801–825. https://doi.org/10.1002/2014JD022617

Huang, J., Golombek, A., Prinn, R., Weiss, R., Fraser, P., Sim-monds, P., et al. (2008). Estimation of regional emissions of nitrous oxide from 1997 to 2005 using multinetwork measurements, a chemical transport model, and an inverse method. *Journal of Geophysical Research*, *113*, D17313. https://doi.org/10.1029/2007JD009381

Intergovernmental Panel on Climate Change (IPCC) (2006). *IPCC guidelines for national greenhouse gas inventories*. Edited by Eggleston S, et al. Hayama, Japan: Institute for Global Environmental Strategies. On the behalf IPCC, National Greenhouse Gas Inventory Program. Retrieved from http://www.ipcc-nggip.iges.or.jp/public/2006gl/index.html

Jeong, S., Zhao, C., Andrews, A. E., Dlugokencky, E. J., Sweeney, C., Bianco, L., et al. (2012). Seasonal variations in N2O emissions from central California. *Geophysical Research Letters*, *39*, L16805. https://doi.org/10.1029/2012GL052307

Ju, X.-T., Xing, G.-X., Chen, X.-P., Zhang, S.-L., Zhang, L.-J., Liu, X.-J., et al. (2009). Reducing environmental risk by improving N management in intensive Chinese agriculture. *Proceedings of the National academy of Sciences of the United States of America*, *106*(9), 3041–3046. https://doi.org/10.1073/pnas.0813417106

Kort, E. A., Andrews, A. E., Dlugokencky, E., Sweeney, C., Hirsch, A., Eluszkiewicz, J., et al. (2010). Atmospheric constraints on 2004 emissions of methane and nitrous oxide in North America from atmospheric measurements and receptor-oriented modeling framework. *Journal of Integrative Environmental Sciences*, *7*, 125–133. https://doi.org/10.1080/19438151003767483

Kort, E. A., Eluszkiewicz, J., Stephens, B. B., Miller, J. B., Gerbig, C., Nehrkorn, T., et al. (2008). Emissions of CH_4 and N_2O over the United States and Canada based on a receptor-oriented modeling framework and COBRA-NA atmospheric observations. *Geophysical Research Letters*, *35*, L18808. https://doi.org/10.1029/2008GL034031

Levis, S., Bonan, G. B., Kluzek, E., Thornton, P. E., Jones, A., Sacks, W. J., & Kucharik, C. J. (2012). Interactive crop management in the Community Earth System Model (CESM1): Seasonal influences on land-atmosphere fluxes. *Journal of Climate*, *25*, 4839–4859. https://doi.org/10.1175/JCLI-D-11-00446.1

Lin, J. C., Gerbig, C., Wofsy, S. C., Andrews, A. E., Daube, B. C., Davis, K. J., & Grainger, C. A. (2003). A near-field tool for simulating the upstream influence of atmospheric observations: The Stochastic Time-Inverted Lagrangian Transport (STILT) model. *Journal of Geophysical Research*, *108*(D16), 4493. https://doi.org/10.1029/2002JD003161

MacFarling Meure, C., Etheridge, D. M., Trudinger, C. M., Steele, L. P., Langenfelds, R. L., van Ommen, T., et al. (2006). Law Dome CO_2, CH_4, and N_2O ice core records extended to 2000 years BP. *Geophysical Research Letters*, *33*, L14810. https://doi.org/10.1029/2006GL026152

Manizza, M., Keeling, R. F., & Nevison, C. D. (2012). On the processes controlling the seasonal cycles of the air-sea fluxes of O_2 and N_2O: A modeling study. *Tellus-B*, *64*, 18429. https://doi.org/10.3402/tellusb.v64i0.18429

Manning, A. J., O'Doherty, S., Jones, A. R., Simmonds, P. G., & Derwent, R. G. (2011). Estimating UK methane and nitrous oxide emissions from 1990 to 2007 using an inversion modeling approach. *Journal of Geophysical Research*, *116*, D02305. https://doi.org/10.1029/2010JD014763

Masarie, K. A., & Tans, P. P. (1995). Extension and integration of atmospheric carbon dioxide data into a globally consistent measurement record. *Journal of Geophysical Research*, *100*(D6), 11,593–11,610. https://doi.org/10.1029/95JD00859

McElroy, M. B., & Wofsy, S. C. (1976). Sources and sinks for atmospheric N_2O. *Reviews of Geophysics*, *14*(2), 143–150. https://doi.org/10.1029/RG014i002p00143

Mesinger, F., DiMego, G., Kalnay, E., Mitchell, K., Shafran, P. C., Ebisuzaki, W., et al. (2006). North American Regional Reanalysis. *Bulletin of the American Meteorological Society*, *87*(3), 343–360. https://doi.org/10.1175/BAMS-87-3-343

Michalak, A. M., Hirsch, A., Bruhwiler, L., Gurney, K. R., Peters, W., & Tans, P. P. (2005). Maximum likelihood estimation of covariance parameters for Bayesian atmospheric trace gas surface flux inversions. *Journal of Geophysical Research*, *110*, D24107. https://doi.org/10.1029/2005JD005970

Miller, S. M., Michalak, A., & Levi, P. J. (2014). Atmospheric inverse modeling with known physical bounds: An example from trace gas emissions. *Geoscientific Model Development*, *7*, 303–315. https://doi.org/10.5194/gmd-7-303-2014

Miller, S. M., Kort, E. A., Hirsch, A. I., Dlugokencky, E. J., Andrews, A. E., Xu, X., et al. (2012). Regional sources of nitrous oxide over the United States: Seasonal variation and spatial distribution. *Journal of Geophysical Research*, *117*, D06310. https://doi.org/10.1029/2011JD016951

Mosier, A. R., Kroeze, C., Nevison, C. D., & Van Cleemput, O. (1998). Closing the global N_2O budget: Nitrous oxide emissions through the agricultural nitrogen cycle. *Nutrient Cycling in Agroecosystems*, *52*(2/3), 225–248. https://doi.org/10.1023/A:1009740530221

Myhre, G., Shindell, D., Bréon, F.-M., Collins, W., Fuglestvedt, J., Huang, J., et al. (2013). Anthropogenic and Natural Radiative Forcing. In T. F. Stocker, et al. (Eds.), *Climate Change 2013: The Physical Science Basis. Contribution of Working Group I to the Fifth Assessment Report of the Intergovernmental Panel on Climate Change* (Chap. 8, pp. 659–740). Cambridge, United Kingdom and New York: Cambridge University Press.

National Centers for Environmental Prediction (2016). Department of Commerce. 2005, updated monthly. *NCEP North American Regional Reanalysis (NARR)*. Research Data Archive at the National Center for Atmospheric Research, Computational and Information Systems Laboratory. Retrieved from http://rda.ucar.edu/datasets/ds608.0/, Accessed† 26 12 2016.

National Oceanic Atmospheric Administration (NOAA) Global Monitoring Division (2017). Interactive Data Visualization. Retrieved from https://www.esrl.noaa.gov/gmd/dv/iadv/, accessed February 2, 2017.

Nehrkorn, T., Eluszkiewicz, J., Wofsy, S., Lin, J., Gerbig, C., Longo, M., & Freitas, S. (2010). Coupled weather research and forecasting–stochastic time-inverted Lagrangian transport (WRF–STILT) model. *Meteorology and Atmospheric Physics*, *107*(1–2), 51–64. https://doi.org/10.1007/s00703-010-0068-x

Nevison, C. D., & Holland, E. A. (1997). A re-examination of the impact of anthropogenically fixed nitrogen on atmospheric N_2O and the stratospheric O_3 layer. *Journal of Geophysical Research*, *102*(D21), 25,519–25,536. https://doi.org/10.1029/97JD02391

Nishina, K., Ito, A., Hanasaki, N., & Hayashi, S. (2017). Reconstruction of spatially detailed global map of NH_4^+ and NO_3^- application in synthetic nitrogen fertilizer. *Earth System Science Data*, *9*(1), 149–162. www.earth-syst-sci-data.net/9/149/2017/doi:10.5194/essd-9-149-2017

Park, S., Croteau, P., Boering, K. A., Etheridge, D. M., Ferretti, D., Fraser, P. J., et al. (2012). Trends and seasonal cycles in the isotopic composition of nitrous oxide since 1940. *Nature Geoscience*, *5*(4), 261–265. https://doi.org/10.1038/ngeo1421

Parton, W. J., Holland, E. A., del Grosso, S. J., Hartman, M. D., Martin, R. E., Mosier, A. R., et al. (2001). Generalized model for NOx and N_2O emissions from soils. *Journal of Geophysical Research*, *106*(D15), 17,403–17,419. https://doi.org/10.1029/2001JD900101

Potter, P., Ramankutty, N., Bennett, E. M., & Donner, S. D. (2010). Characterizing the spatial patterns of global fertilizer application and manure production. *Earth Interactions*, *14*(2).

Prather, M. J., Hsu, J., DeLuca, N. M., Jackman, C. H., Oman, L. D., Douglass, A. R., et al. (2015). Measuring and modeling the lifetime of nitrous oxide including its variability. *Journal of Geophysical Research: Atmospheres*, *120*, 5693–5705. https://doi.org/10.1002/2015JD023267

Prinn, R. G., Weiss, R. F., Fraser, P. J., Simmonds, P. G., Cunnold, D. M., Alyea, F. N., et al. (2000). A history of chemically and radiatively important gases in air deduced from ALE/GAGE/AGAGE. *Journal of Geophysical Research*, *105*(D14), 17,751–17,792. https://doi.org/10.1029/2000JD900141

Ramankutty, N., & Foley, J. A. (1998). Characterizing patterns of global land use: An analysis of global croplands data. *Global Biogeochemical Cycles*, *12*, 667–685.

Ravishankara, A., Daniel, J., & Portmann, R. (2009). The dominant ozone-depleting substance emitted in the 21st century. *Science*, *326*(5949), 123–125. https://doi.org/10.1126/science.1176985

Saikawa, E., Prinn, R. G., Dlugokencky, E., Ishijima, K., Dutton, G. S., Hall, B. D., et al. (2014). Global and regional emissions estimates for N_2O. *Atmospheric Chemistry and Physics*, *14*(9), 4617–4641. https://doi.org/10.5194/acp-14-4617-2014

Saikawa, E., Schlosser, C. A., & Prinn, R. G. (2013). Global modeling of soil nitrous oxide emissions from natural processes. *Global Biogeochemical Cycles*, *27*, 972–989. https://doi.org/10.1002/gbc.20087

Stein, A. F., Draxler, R. R, Rolph, G. D., Stunder, B. J. B., Cohen, M. D., & Ngan, F. (2015). NOAA's HYSPLIT atmospheric transport and dispersion modeling system. *Bulletin of the American Meteorological Society*, *96*, 2059-2077. https://doi.org/10.1175/BAMS-D-14-00110.1 this link opens in a new window

Stephens, B. B., Gurney, K. R., Tans, P. P., Sweeney, C., Peters, W., Bruhwiler, L., et al. (2007). Weak northern and strong tropical land carbon uptake from vertical profiles of atmospheric CO_2. *Science*, *316*(5832), 1732–1735. https://doi.org/10.1126/science.1137004

Stohl, A., Hittenberger, M., & Wotawa, G. (1998). Validation of the Lagrangian particle dispersion model FLEXPART against large scale tracer experiments. *Atmospheric Environment*, *32*(24), 4245–4264. https://doi.org/10.1016/S1352-2310(98)00184-8

Sweeney, C., Karion, A., Wolter, S., Newberger, T., Guenther, D., Higgs, J. A., et al. (2015). Seasonal climatology of CO_2 across North America from aircraft measurements in the NOAA/ESRL Global Greenhouse Gas Reference Network. *Journal of Geophysical Research: Atmospheres*, *120*, 5155–5190. https://doi.org/10.1002/2014JD022591

Thompson, R. L., Ishijima, K., Saikawa, E., Corazza, M., Karstens, U., Patra, P. K., et al. (2014). TransCom N_2O model inter-comparison Part 2: Atmospheric inversion estimates of N_2O emissions. *Atmospheric Chemistry and Physics*, *14*(12), 6177–6194. https://doi.org/10.5194/acp-14-6177-2014

Thompson, T. M., Elkins, J. W., Hall, B., Dutton, G. S., Swanson, T. H., Butler, J. H., et al. (2004). Halocarbons and other atmospheric trace species. In R. C. Schnell, A.-M. Buggle, & R. M. Rossson (Eds.), *Climate Diagnostics Laboratory Summary Report #27, 2002–2003*. Boulder, CO: Department of Commerce, National Oceanic and Atmospheric Administration.

Vitousek, P. M., Aber, J., Howarth, R. W., Likens, G. E., Matson, P. A., Schindler, D. W., et al. (1997). Human alterations of the global nitrogen cycle: Causes and consequences. *Ecological*, *1*, 1–15.

Vitousek, P. M., Naylor, R., Crews, T., David, M. B., Drinkwater, L. E., Holland, E., et al. (2009). Nutrient imbalances in agricultural development. *Science*, *324*(5934), 1519–1520. https://doi.org/10.1126/science.1170261

Wagner-Riddle, C., Congreves, K. A., Abalos, D., Berg, A. A., Brown, S. E., Ambadan, J. T., et al. (2017). Globally important nitrous oxide emissions from croplands induced by freeze–thaw cycles. *Nature Geoscience*. https://doi.org/10.1038/NGEO2907

Xiang, B., Miller, S. M., Kort, E. A., Santoni, G. W., Daube, B. C., Commane, R., et al. (2013). Nitrous oxide (N_2O) emissions from California based on 2010 CalNex airborne measurements. *Journal of Geophysical Research: Atmospheres*, *118*, 2809–2820. https://doi.org/10.1002/jgrd.50189

Yadav, V., & Michalak, A. M. (2013). Improving computational efficiency in large linear inverse problems. *Geoscientific Model Development*, *6*(3), 583–590. https://doi.org/10.5194/gmd-6-583-2013